Titre: Title:	Blackbox Optimization for Origami-Inspired Bistable Structures
Auteur: Author:	Luca Pierre Jean Claude Boisneault
Date:	2024
Type:	Mémoire ou thèse / Dissertation or Thesis
Référence: Citation:	Boisneault, L. P. J. C. (2024). Blackbox Optimization for Origami-Inspired Bistable Structures [Mémoire de maîtrise, Polytechnique Montréal]. PolyPublie. https://publications.polymtl.ca/59459/

POLYTECHNIQUE MONTRÉAL
affiliée à l'Université de Montréal

Blackbox Optimization for Origami-Inspired Bistable Structures

LUCA PIERRE JEAN CLAUDE BOISNEAULT
Département de génie mécanique

Mémoire présenté en vue de l'obtention du diplôme de *Maîtrise ès sciences appliquées*
Génie aérospatial

Septembre 2024

POLYTECHNIQUE MONTRÉAL
affiliée à l'Université de Montréal

Ce mémoire intitulé :

Blackbox Optimization for Origami-Inspired Bistable Structures

présenté par **Luca Pierre Jean Claude BOISNEAULT**
en vue de l'obtention du diplôme de *Maîtrise ès sciences appliquées*
a été dûment accepté par le jury d'examen constitué de :

Alain BATAILLY, président
David MÉLANÇON, membre et directeur de recherche
Charles AUDET, membre et codirecteur de recherche
Youssef DIOUANE, membre

ACKNOWLEDGEMENTS

I would first like to thank my research supervisors, Charles Audet and David Mélançon, for their support and the incredible opportunity they offered me during these two years of my Master's program.

Beginning a new adventure on the other side of the world was not always easy, but I found in them a source of motivation to persevere and complete my academic journey. Their commitment to the well-being of their students, both at Polytechnique and outside the academic setting, was greatly appreciated and was a driving force behind the success of my project.

I would also like to thank my colleagues who started their Master's program at the same time as I did: Yannis Liétard, Josua Garon, and Danick Lamoureux. The moments spent with you will remain in my memory for a long time. I wish them all the best in their future endeavors, and I am sure that we will meet again in the future.

I would like to thank all the PhD, Master's, Bachelor's students, and interns I had the chance to meet at LM^2 and GERAD. I was fortunate enough to be part of two of the most active laboratories at Polytechnique, and I hope the atmosphere will remain the same for many years to come. My Master's experience wouldn't have been the same without the discussions, meals, sports activities, and evenings spent with you. Thank you for making my days so fulfilling.

I would like to thank the jury members, Alain Batailly and Youssef Diouane, for their constructive comments and the discussions about my work, which were greatly appreciated.

Finally, I want to thank all the people with whom I have developed great friendships since my arrival in Montreal. Expeditions, bike rides, networking activities, parties, your support over the past two years has meant a lot to me, and I couldn't have continued my journey in the same way without you. Thank you all.

RÉSUMÉ

La bistabilité définit la capacité d'une structure à prendre deux configurations stables, où son énergie élastique est minimisée localement. L'origami représente une source d'inspiration pour concevoir des structures déployables possédant à la fois une configuration compacte et une autre déployée, avec une fonctionnalité différente. L'étape de déploiement de l'origami peut faire émerger de la bistabilité par la déformation des composantes mécaniques. En théorie, les structures inspirées de l'origami sont représentées comme des surfaces connectées entre elles par des lignes de pivot idéales et sans rigidité. Dans ce cas, les deux états stables sont des minima globaux de la fonction d'énergie élastique. En pratique, les structures sont fabriquées dans l'un des deux états stables et avec une rigidité non nulle au niveau des zones de pliage. Après déploiement, des contraintes résiduelles subsistent dans le mécanisme, entraînant une diminution de la performance dans l'un des deux états d'équilibre. Pour résoudre ce problème, il est possible d'améliorer cette performance mécanique en effectuant un processus d'optimisation sur la définition générale du motif d'origami, et sur les détails des géométries qui effectuent le pliage. Il s'agit de trouver le motif d'origami qui maximise la performance bistable, que l'on définit comme la quantité d'énergie normalisée nécessaire pour passer d'un état à un autre, tout en conservant une contrainte mécanique qui permet le déploiement sans briser la structure. Dans cette étude, l'algorithme Mesh Adaptive Direct Search (MADS), une méthode d'optimisation sans dérivées pour résoudre des problèmes de boîtes noires, est utilisé pour la résolution. Le motif origami de la Bombe à eau (Waterbomb pattern) est sélectionné pour démontrer la pertinence de l'optimisation menée. L'énergie élastique au cours du déploiement est calculée par la méthode des éléments finis et servira de boîte noire dans la boucle d'optimisation. Les géométries optimisées du modèle numérique sont fabriquées par impression 3D et validées expérimentalement sur une machine de traction. Cette procédure se veut être une méthodologie générale applicable aux motifs d'origami bistables et utilisable dans tout domaine d'ingénierie.

ABSTRACT

Deforming a mechanical system with a constant load usually induces a monotonic rise in the stored elastic energy. Structures with specific geometries are known to be capable of overcoming this principle, and their stored energy will eventually decrease after a certain displacement. The resulting displacement-energy curves will display more than one position where the elastic energy is locally minimized, and the minimum potential energy principle implies that the positions in which the elastic energy is minimized are stable configurations of the structures. This "lock in place" property finds many applications in deployable structures, reconfiguration mechanisms, or to store energy. Interest in origami, the Japanese art of paper folding, has risen over the last decades in engineering applications for the benefits brought by the embedded hinges and the associated kinematics. Some researchers have put forward the capacity of several origami patterns to display bistable, or multistable, behaviors, thus providing more than one useful geometrical configuration. Manufacturing methods for origami imply that one of the stable states will be a global minimum of the energy landscape, but this is not the case for the other stable states: residual stress remains after deformation, leading to a non-zero energy state. This means that the energy barrier one needs to overcome to leave the equilibrium position is not the same for every state. In this work, a coupled Finite Element-Blackbox optimization framework is presented to reduce the remaining stored energy in the equilibrium positions, i.e., increase bistability performance. It is intended to be applicable to any parameterized bistable system, and a focus on the Waterbomb pattern is presented to demonstrate the benefit obtained through our method. Samples are fabricated using multimaterial 3D printing and tested experimentally under point loading in a tensile testing machine to validate our numerical results.

TABLE OF CONTENTS

LIST OF FIGURES

LIST OF SYMBOLS AND ACRONYMS

Acronym

BB	Blackbox
CAD	Computer-aided Design
DFO	Derivative-Free Optimization
FEM	Finite Element Method
FFF	Fused Filament Fabrication
MADS	Mesh Adaptative Direct Search
NOMAD	Nonlinear Optimization with the MADS algorithm
PLA	Polylactic Acid
TPU	Thermoplastic polyurethane

Symbols

n	Number of axial symmetry of the waterbomb pattern
h	Height of the waterbomb pattern in the first state
r_o	Outer radius of the waterbomb patter
r_i	Inner radius of the waterbomb patter
δ	Central node displacement
ΔU	Energy well depth
$U_{\max}$	Maximum of energy separating the two stable states
ϕ	Bistability performance
E_f	Young's Modulus of the facets
E_c	Young's Modulus of the creases
ν_f	Poisson's ratio of the facets
ν_c	Poisson's ratio of the creases
ρ_f	Density of the facets
ρ_c	Density of the creases
S_Y^f	Yield strength of the facets
S_Y^c	Yield strength of the creases
t_f	Thickness of the facets
t_c	Thickness of the creases
w	Ratio of thickness

θ_i	Angle defining the waterbomb pattern
$\sigma_{\max}$	Maximum of mechanical stress happening during the actuation phase
x_i	Input vector of the blackbox
l_b	Lower boundary of the optimization problem
u_b	Upper boundary of the optimization problem

CHAPTER 1 INTRODUCTION

1.1 Context

Packaging boxes, satellites, mechanical metamaterials, origami offers a new framework for engineering design, from the millimeter [86] to the meter scale [62]. The main advantages of origami are the possibilities for shape-shifting, often leading to the design of systems comprising both a folded and a deployed configuration [61], structures with multiple useful configurations [43], or even a continuous range of action to achieve specific displacements [82]. Various numerical methods are being developed to better understand the kinematics and the mechanical deformations at play [93]. New patterns can emerge by using generative algorithms [25, 26], and the advantages of their reconfiguration and foldability have started reaching our day-to-day objects.

Deforming a mechanical system usually induces a rise in elastic energy stored within the material. However, some geometries behave in such a way that after imposing a specific displacement, the elastic energy starts decreasing. For this case, energy-actuation curve exhibits two local minima, i.e., two configurations in which the system wants to remain. This is referred to as bistability, or more generally, multistability in the case of more than two equilibrium states.

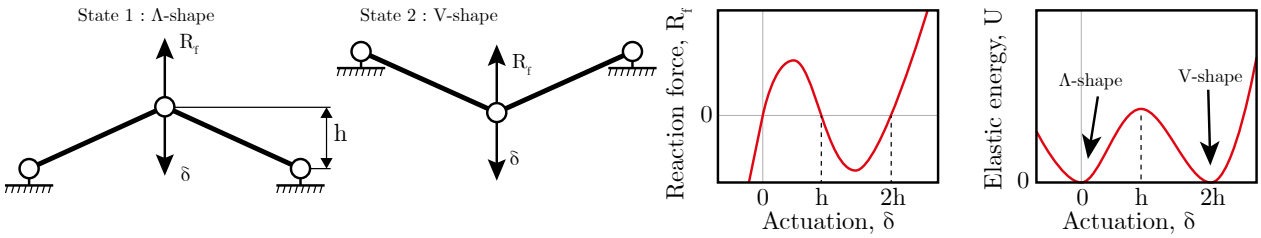

Figure 1.1 **Behavior of the bistable von Mises truss :** Both equilibrium are represented as well as the force and energetic response of the system under punctual displacement.

The simplest mechanical structure displaying this bistability is an assembly of two trusses, connected in a Λ-shape by a ball joint link, and to the ground at their other end using the same type of connection. This system is known as the "von Mises truss" [19], and when the apex of the structure is pulled downward, the trusses will first compress and increase their elastic energy before eventually releasing energy after a displacement corresponding to the height of the initial apex as shown in Figure 1.1. The system will then snap into a second equilibrium position, forming a V-shape. Bistability is not specific to truss structures and

can be achieved with any type of system experiencing deformation, such as origami. The highest amount of elastic energy separating two states is referred to as the energy barrier, which characterizes the performance of a bistable structure: the higher the energy barrier, the more deformation is needed to switch to a different state.

Combining origami engineering with multistability enables designers to create structures capable of locking in specific positions by harnessing the deformation occurring during deployment. This way, origami-inspired multistable structures do not need to rely on traditional locking mechanisms to remain in the desired configuration.

Because systems are built in one of the stable states, the elastic energy in this configuration is zero. When deformed into one of the other states, some residual stress induced by the deformation remains, and the configuration is not energetically neutral. This leads to some stable states being more energetically favorable than others. Understanding the elastic energy and its distribution within the structure is key to designing efficient mechanical systems. Adjusting the origami pattern geometry may reduce the residual stress and restore lost performance.

1.2 Motivation

Research in origami exhibits how versatile origami-inspired multistable structures are, with the development of projects in aerospace engineering [94, 34], medical devices [45], and robotics [70], to name a few. However, designs proposed in the literature are mostly proof-of-concepts.

The only works that tried to enhance multistability focused on the general pattern of origami structure to maximise the energy barrier. To design efficient bistable origami systems, one has to take into account the geometry of the deforming regions, i.e, the hinges, as well as the associated manufacturing limits. This work aims at providing a rigorous process to optimize bistability and to show that the lost performance can be retrieved using geometrical tuning.

1.3 Organization

This Master's thesis is divided into five additional chapters. In Chapter 2, a literature review on origami engineering is presented, including mathematical formulations, simulation tools, fabrication processes and actuation methods. In addition, a more complete definition of multistability is provided, as well as an overview of blackbox optimization methods, along with their advantages and applications to engineering projects that present constraints similar to

those encountered in origami engineering. The literature review synthesis and the project objectives are discussed in Chapter 3. Chapter 4 reproduces the research article titled "Black-box optimization for origami-inspired bistable structures" which was submitted to Extreme Mechanics Letters. Chapter 5 addresses additional information on the project such as the details of the fabrication methods and additional optimized geometries. Finally, Chapter 6 closes with a summary of the project, results, and future perspectives.

CHAPTER 2 LITERATURE REVIEW

This Master's project lies within the spectrum of a broad range of innovative concepts, both in mechanical engineering and mathematical optimization. A summary of research in origami engineering is presented, along with the advantages gained when combined with bistability. Numerical modeling of origami-inspired structures is discussed, as it must be considered to ensure the reliability of the computed data. Finally, derivative-free and blackbox optimization methods are introduced as efficient tools to enhance the performance of multistable systems.

2.1 Origami in engineering

2.1.1 Rigid-foldable origami

Inspired by the Japanese art of paper folding, researchers have designed structures that encapsulate multiple feasible shapes. Rigid origami is the branch of origami engineering that describes structures as an assembly of planar, non-deformable facets connected along straight lines that allow rotation. Here, the focus is on the kinematics of the structure, and the complete motion can be studied by solving the equations of motion. Most projects are based on popular patterns such as the Waterbomb, Miura-Ori, and Yoshimura as shown in Figure 2.1.

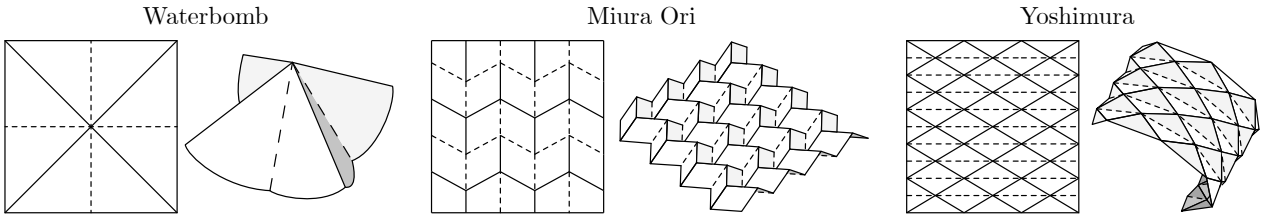

Figure 2.1 **Pattern of the Waterbomb, Miura Ori, and Yoshimura origami as used in the rigid-foldable framework**

Rigid-foldable origami is commonly used in applications where the structural integrity of the facets is crucial. For example, in aerospace, structures inspired by the Miura-Ori [80] can be folded during launch into space, later deployed for energy production as solar arrays [94] or communication antennas [34]. These aerospace applications are shown in Figure 2.2a-c. Civil engineering can also benefit from origami to design deployable structures that can collapse on themselves [62] (Figure 2.2d) or modular large-scale structures that can adapt to their environment [92]. Origami engineering is also practical for everyday tasks like folding

shopping bags [83] (Figure 2.2e) or providing dynamic forms of art [77].

Similar to traditional origami, many researchers study the behavior of origami without considering the thickness of the material [71, 76]. However, for thick origami, the position of the hinge must be accounted for to avoid collision between the panels, whether using rolling hinges [46] (Figure 2.2f) or ideal pivots [92].

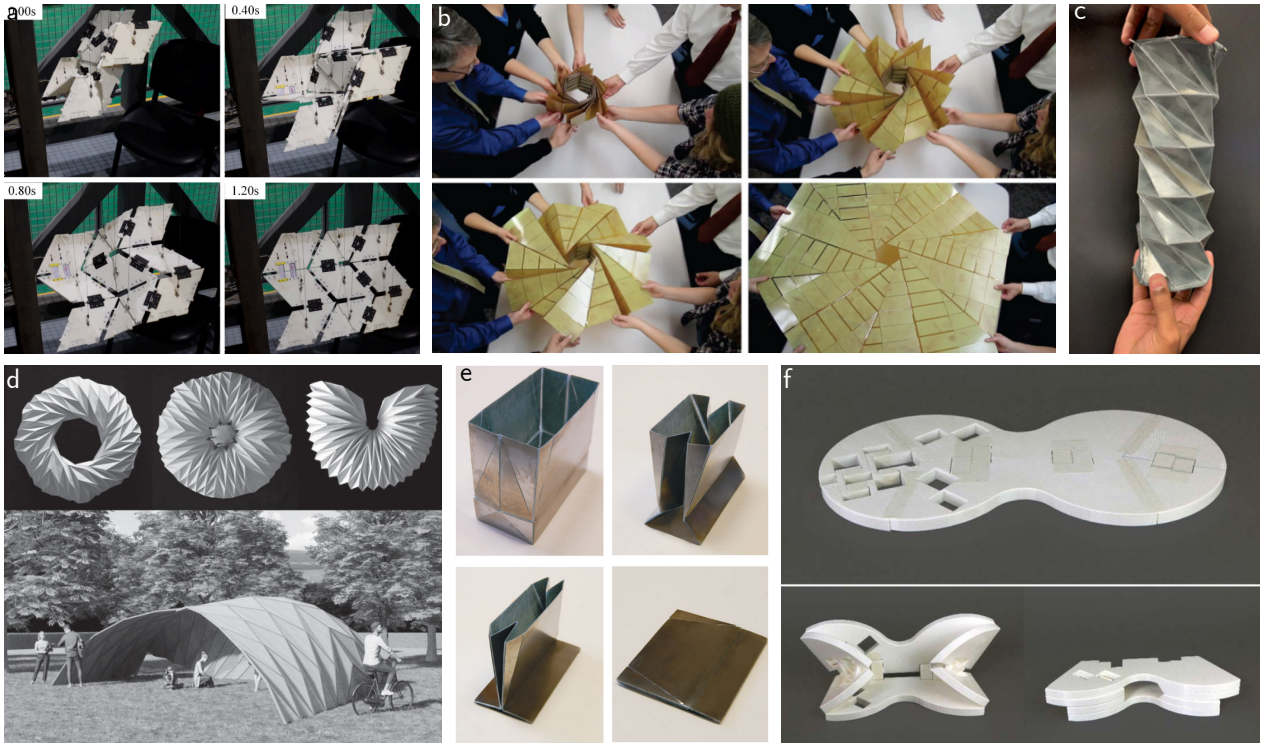

Figure 2.2 **Examples of rigid-foldable origami a.** Release of a spring-loaded Miura-Ori [80]. **b.** HanaFlex solar array transitioning from folded to deployed configuration [94]. **c.** Deployable antenna based on the Kresling pattern [34]. **d.** Application of the Yoshimura pattern in civil engineering [62]. **e.** Using origami to fold shopping bags [83]. **f.** Thick origami folded using rolling hinges [46].

2.1.2 Deformable origami

In deformable origami, the facets are no longer considered infinitely rigid, and previously non-rigid-foldable patterns can now be deployed [73]. Flexibility can be achieved by changing the fabrication material, geometrical parameters in the pattern, or by implementing new boundary conditions with the environment. Examples of deformable origami-inspired structures are shown in Figure 2.3. Thanks to flexibility, origami can now extend its range of applications. Based on the Kresling pattern, researchers have designed an octopus-like robotic arm capable of bending in response to an applied magnetic field [82] as shown in Figure 2.3a.

Such deformation would not be possible with a rigid-foldable origami formulation. Figure 2.3b displays a second robotic arm capable of bending and twisting motions, fitted with a gripper [15]. Structures can also be stored in a geometrically frustrated configuration, as in the case of an origami-inspired wing in Figure 2.3c. When released, the system acts as a spring, effectively deploying the structure to the desired shape [27].

Origami structures can enable enable effective load distribution, as well as adaptability to various stresses. In Figure 2.3d, an origami muscle weighing only a few grams is able to lift a kilogram when placed under pressure [50]. Large origami structures that can shelter several people are deployed through origami (see Figure 2.3e) [60]. Deformation also allows for greater flexibility, and the gripper based on the waterbomb pattern shown in Figure 2.3f can conform to the shape of objects to better grasp them.

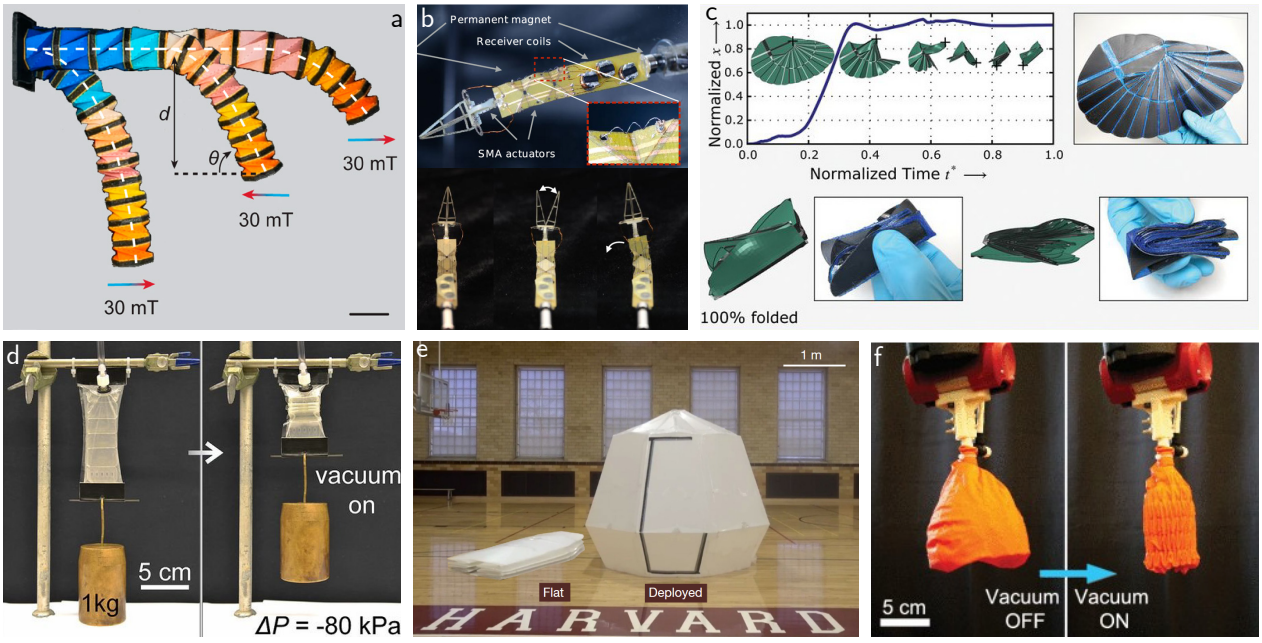

Figure 2.3 **Examples of deformable origami-inspired engineering structures** **a.** Kresling-based omnidirectional robotic arm [82]. **b.** Origami gripper at the millimeter scale [15]. **c.** Folded and deployed configuration of an origami-inspired wing [27]. **d.** Fluid-actuated muscle using origami to lift weight [51]. **e.** Deployable origami shelter [61]. **f.** Vacuum-actuated waterbomb-based gripper [50].

2.1.3 Simulating origami-inspired structures

Simulation in origami engineering depends on the type of structure being studied, whether rigid or deformable. In the case of rigid structures, the focus is on determining the kinematics during deployment or reconfiguration of the pattern. In some cases, such as the Miura-Ori,

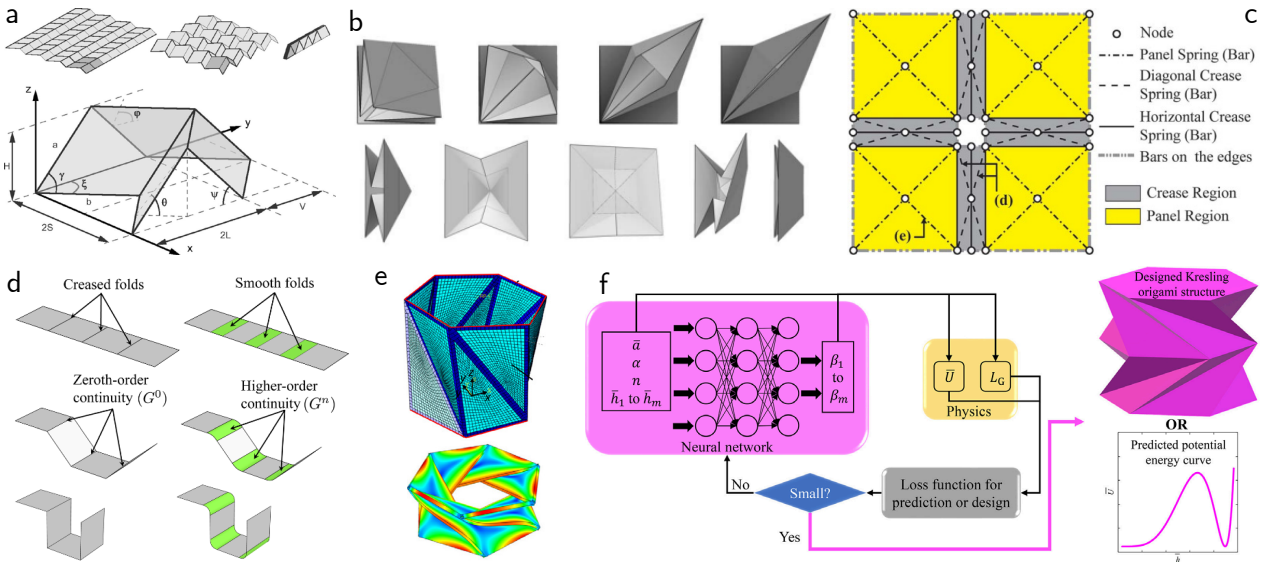

Figure 2.4 **Computational models for origami engineering a.** Single DOF deployment of the rigid Miura-Ori [71]. **b.** FreeForm Origami software to predict folding of origami patterns [76]. **c.** SWOMPS bars and hinges model [90]. **d.** Enhanced continuity of origami patterns using compliant crease modeling [69]. **e.** Finite Element Analysis applied to Kresling spring origami folding, showing the stress field under compression [23]. **f.** PINN used to predict the behavior of the Kresling pattern [52].

a single degree of freedom (translation or rotation) can define the complete motion of the structure [71] (Figure 2.4a). More complex patterns require a sequence of folding steps, and each equation of motion must be solved to determine the full kinematics. Software has been developed to predict and simulate each folding step [76] (Figure 2.4b).

For deformable origami, varying levels of complexity are considered to predict deformations. Discrete models (often referred to as "bars and hinges models") replace the surface panels with bar and spring elements to capture bending and stretching of origami structures during deployment [90], as shown in Figure 2.4c. The total energy U_{tot} of the origami pattern is computed as the sum of the energy stored in each bar through traction or compression and in each spring through rotation, as shown in equation 2.1:

$$U_{tot} = \sum^{i} U_{bar} + \sum^{j} U_{spring}, \tag{2.1}$$

where i the number of bar elements, and j the number of spring elements in the model. Following the minimum total energy principle, U_{max} is then minimized with regard to its degrees of freedom to find the kinematics of the structure. Folding regions can be simulated as perfect pivots or as softer regions, i.e., compliant creases embedded in a structure with

other stiffer regions. This second method also allows for a higher degree of continuity in the pattern [69]. It can be implemented in discrete models by assigning less rigidity to some spring and bar elements to mimic the behavior of a softer region between facets. Bar and hinge models are a fast way of approximating deformation in origami. The Finite Elements Method (FEM) can also be used, with several approaches available: a similar approach as bar and hinge models with 1D elements, a shell formulation (2D elements) for a better understanding of the overall deformation [23] (Figure 2.4e), and even further with 3D elements if one needs to understand the phenomena occurring in the folding region of the structure and in the thickness of the facets.

Recent research in the field of mechanical simulation has introduced new approaches based on a combination of physical models and neural networks, called Physics-Informed Neural Networks (PINNs) (Figure 2.4f). Promising results have shown that the deployment-energy curve of complex origami patterns can be predicted within seconds [52].

2.1.4 Fabrication of Origami

The word "origami" comes from Japanese, combining "ori", which means folding, and "gami", which means paper. In origami engineering, researchers experiment with a wide range of materials and fabrication techniques to adapt to specific needs, whether to fulfill structural requirements or to induce precise displacements.

The main requirement for origami-inspired structures is to allow folding on well-defined regions. Designing folding regions and connecting them to more rigid facets in origami engineering is challenging. Multi-material fabrication has been proposed with inter-material bonding to ensure efficient adhesion between each part. Laminates of composite materials have been employed, ranging from cardboard with adhesive [67] for simple and cheap prototyping in centimeter-scale structures (Figure 2.5a) to carbon fiber composites [75, 24], for more precise mechanical systems such as in a medical device for precision tasks (Figure 2.5b).

Elastomeric molded materials with embedded stiffeners and fluid channels enable inflation as a method of actuation. For example, in Figure 2.5c, an origami-inspired gripper uses inflation to apply pressure on objects. Fused filament 3D printing has also been extensively used because it allows for fast prototyping, can process both soft and rigid materials, and the manufactured geometry can be directly outputted from a CAD model, enabling higher fidelity to the numerical model. Typically, Thermoplastic polyurethane (TPU) is used for the creases due to its flexible properties, combined with Polylactic acid (PLA) or Acrylonitrile butadiene styrene (ABS), materials that can be easily shaped with any printer due to their low melting temperatures, as shown in Figure 2.5d. Chemical bonding between these materials [16] is

sufficient, but additional work on geometry can be done to improve connections, either by wrapping [85] or by using interlaced slicing [44].

Mono-material methods can also be employed with weaknesses embedded in the geometry to create hinges. This has been achieved on paper-like materials using laser cutting [84] (Figure 2.5e). Rotational hinges connecting stiff materials like wood can be used if one wants to remain in the rigid-foldable framework [92] (see Figure 2.5f).

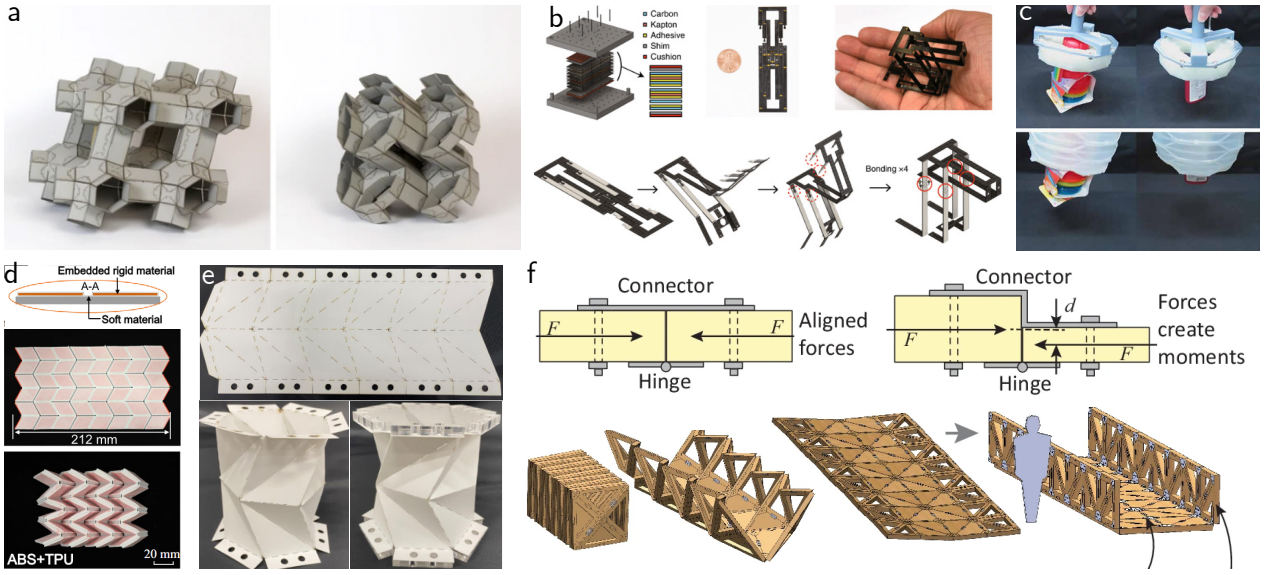

Figure 2.5 **Fabrication methodology for origami engineering a.** Cardboard-adhesive laminate manufacturing [67]. **b.** Millimeter origami robot based on laminate [75]. **c.** Inflatable origami made of molded polymer used to grab different objects [43]. **d.** 3D printed self-locking origami metamaterial [85]. **e.** Laser-cut paper to build a Kresling origami [84]. **f.** Large-scale origami based on thick wooden panels and rotational hinges [92].

2.1.5 Actuating Origami

Actuation in origami requires triggering specific hinges for a given motion. This process can be performed using only one mechanical input or through a sequence of steps. External inputs, such as fluid pressure [61, 50] or the displacement of a defined node [37], can be used. Origami structures can also embed mechanisms within their internal structure (in the facets or the hinges). These mechanisms can range from fluidic channels allowing for air pressure flow through the structure [64] (Figure 2.6a) to heat-responsive materials [30] (Figure 2.6b) and even magnetic fields [21, 82] (Figure 2.6c). Multiple energy sources can be used to actuate the same structure, as demonstrated by Fang et al. [29] (see Figure 2.6d), which uses air pressure, an electrical motor, and shape memory alloys to set an earthworm-like robot in

motion based on the waterbomb pattern.

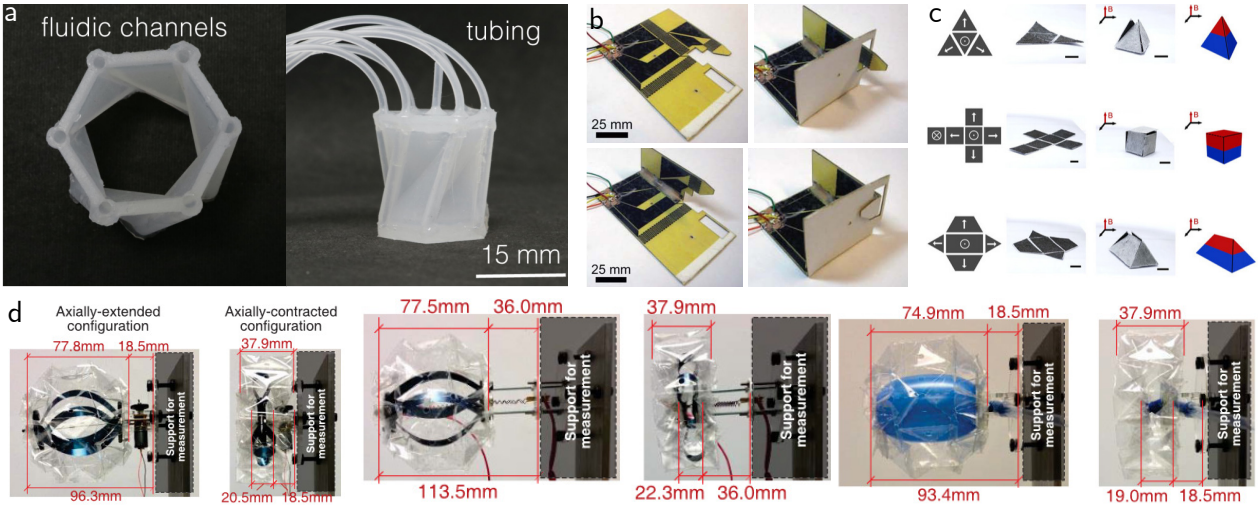

Figure 2.6 **Actuation methods in origami engineering a.** Inflatable channels in the hinges of the Kresling pattern [64]. **b.** Shape Memory Alloy (SMA) to fold origami [30]. **c.** Magnetic fields and their orientation to fold structures [21]. **d.** Earthworm origami robot actuated using inflation, motors, and SMA springs [29].

2.2 Multistability and bistability in mechanical systems

The elastic energy curve of a mechanical system can be evaluated by measuring the force-displacement curve at points of imposed displacement. The corresponding elastic energy response can then be estimated using the formula:

$$U(\delta) = \int_0^{\delta} F(x)\,\mathrm{d}x. \tag{2.2}$$

This quantity is similar to the definition of mechanical work required to actuate the mechanism.

There are three possible scenarios for any mechanical system under punctual loading. First, the reaction force can display a monotonic behavior, where the amplitude of the force keeps increasing with the displacement. Hookean materials exhibit this behavior in their elastic regime, causing the elastic energy of the structure to continually increase (Figure 2.7a).

In the second case, a structure may experience a reduction in the amplitude of the reaction force without a change in the sign of the force. This affects the rate at which the energy increases but does not alter the monotonic behavior of the elastic energy (Figure 2.7b). Such an effect can be observed in the traction test of ductile materials just before fracture, a

phenomenon referred to as necking in metallic materials.

The last scenario involves a change in the force sign, where the amplitude of the force becomes negative. When the reaction force switches sign, the elastic energy starts decreasing, and the energy curve will have more than one local minimum (Figure 2.7c). This phenomenon is referred to as bistability, and generalized as multistability when there are more than two equilibrium positions, as in Figure 2.7d. Because a mechanical system always aims to minimize its stored energy, the displacement associated with the local minimum represents an equilibrium state, meaning the structure will hold its position unless a displacement sufficient to overcome the energy barrier is applied. This represents an innovative alternative for locking structures into defined shapes.

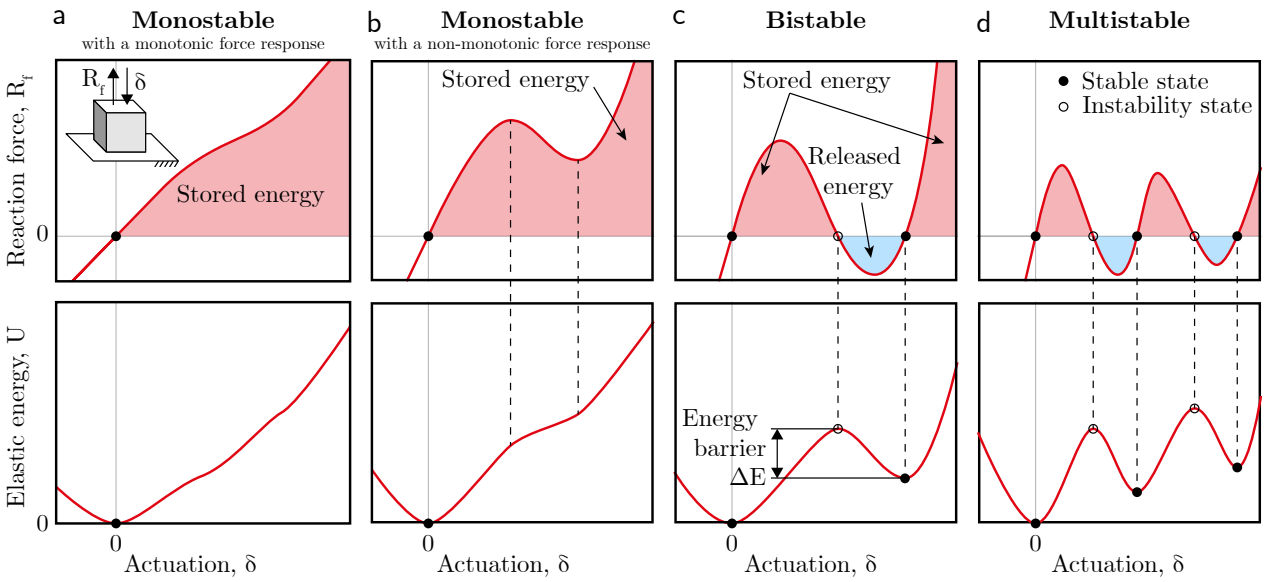

Figure 2.7 **Force and energy response for mechanical system under membrane strain a.** Case a monotonic force response. **b.** Non-monotonic force response and the associated stored energy. **c.** Bistable behavior. **d.** Force and energy response in the case of a multistable structure.

Two types of multistable structures can be identified. First, **beam and truss-based structures** rely on the membrane effect of trusses during deployment to trigger a self-locking mechanism. A beam formulation can also be used to account for flexion and buckling instabilities. Large deployable supporting structures have been developed to hold large protective covers, as shown in Figure 2.8a [2]. The simplest 1D element-based multistable system is the von Mises truss, which has been used to create architected metamaterials capable of trapping elastic energy [72]. This is useful for energy absorption systems, as illustrated in Figure 2.8b, where the referred metamaterial is shown both before and after compression,

effectively increasing the stored energy.

In the second category, **surface-based structures** group all multistable systems relying on 2D elements. This category includes origami [60, 37, 74], kirigami (the art of cutting paper) [68], and simple buckling surfaces [36]. Multistability enables origami structures to rely solely on deformation to lock the system in place. For example, the waterbomb pattern (Figure 2.8c) is a cone-like geometry that can snap into an almost symmetrical configuration after a specific displacement of the cone's apex [37]. Origami is often used to design systems that reduce volume for storage, and multistability enables self-locking in both compact and deployed shapes, as shown in Figure 2.8d. Multistability has also been used to trigger shape-shifting in origami structures, allowing changes in motion enabled by the system. For instance, a robot arm can be controlled with a single fluid pressure input [60] (see Figure 2.8e for a bistable building block of the robot arm). Metamaterials explore the possibilities of 2D elements, as demonstrated by bistable hinges in Figure 2.8f, which can switch between two types of folds (mountain or valley) [41].

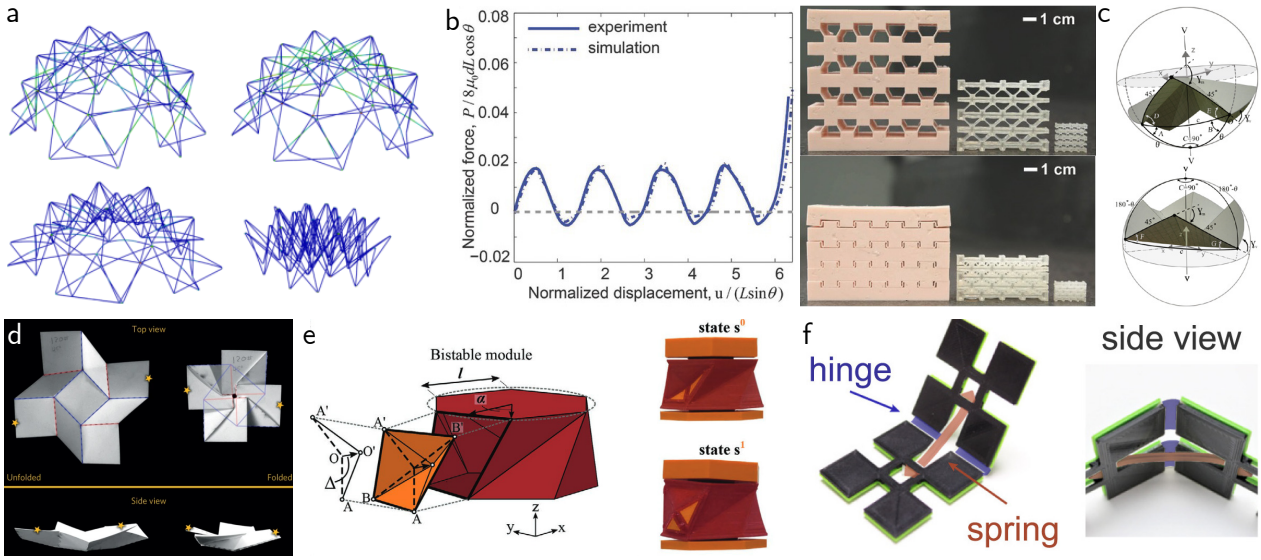

Figure 2.8 **Example of multistability in engineering systems a.** Scissor-beam based deployable structure [2]. **b.** Multistable metamaterial composed of multiple layers of bistable beams [72]. **c.** Waterbomb origami fold, a bistable pattern [37]. **d.** Square twist pattern [74]. **e.** Bistable module to control an origami-inspired robot arm [60]. **f.** Bistable hinge for origami metamaterial [41].

2.3 Blackbox optimization methods

Optimization involves finding the minimum or maximum values of a given function on a specified set. Such problems can be formulated as :

$$\begin{aligned} \max_{x \in \mathbb{R}^n} \quad & f(x) \\ \text{s.t.} \quad & c_i(x) \leq 0 \\ & l_b \leq x \leq u_b. \end{aligned} \tag{2.3}$$

where $f : \mathbb{R}^n \to \mathbb{R} \cup \{\infty\}$ is the objective function and $c :\to (\mathbb{R} \cup \{\infty\})^m$ are functions with $c = (c_1, c_2, \ldots, c_m)$, the mathematical constraints of the problem. Here, the output of the objective and constraint functions can take infinite values to represent hidden constraints [20, 48], for example, the NaN output computed by numerical simulations. Many methods are gradient-based and rely on derivatives to find the optimal function value. However, for some functions, derivatives cannot be used, either due to high computation time [55] or non-smoothness [3], which includes situations where functions are not differentiable, stochastic or not well defined. For such cases, Derivative-free Optimization (DFO) methods are employed [7, 22]. If derivatives are available for a given problem, gradient-based methods should be used due to their higher efficiency.

In blackbox (BB) problems, only the input x and the output $\{f(x), c_i(x)\}$ of the function are known, where $c_i(x)$ are mathematical constraints related to the problem. Any process linking these values is either inaccessible or disregarded. Interest in blackbox optimization has increased in recent years due to its ability to solve computationally expensive problems or those with a high failure rate during evaluation [1]. BB optimization is particularly useful for simulation-based functions.

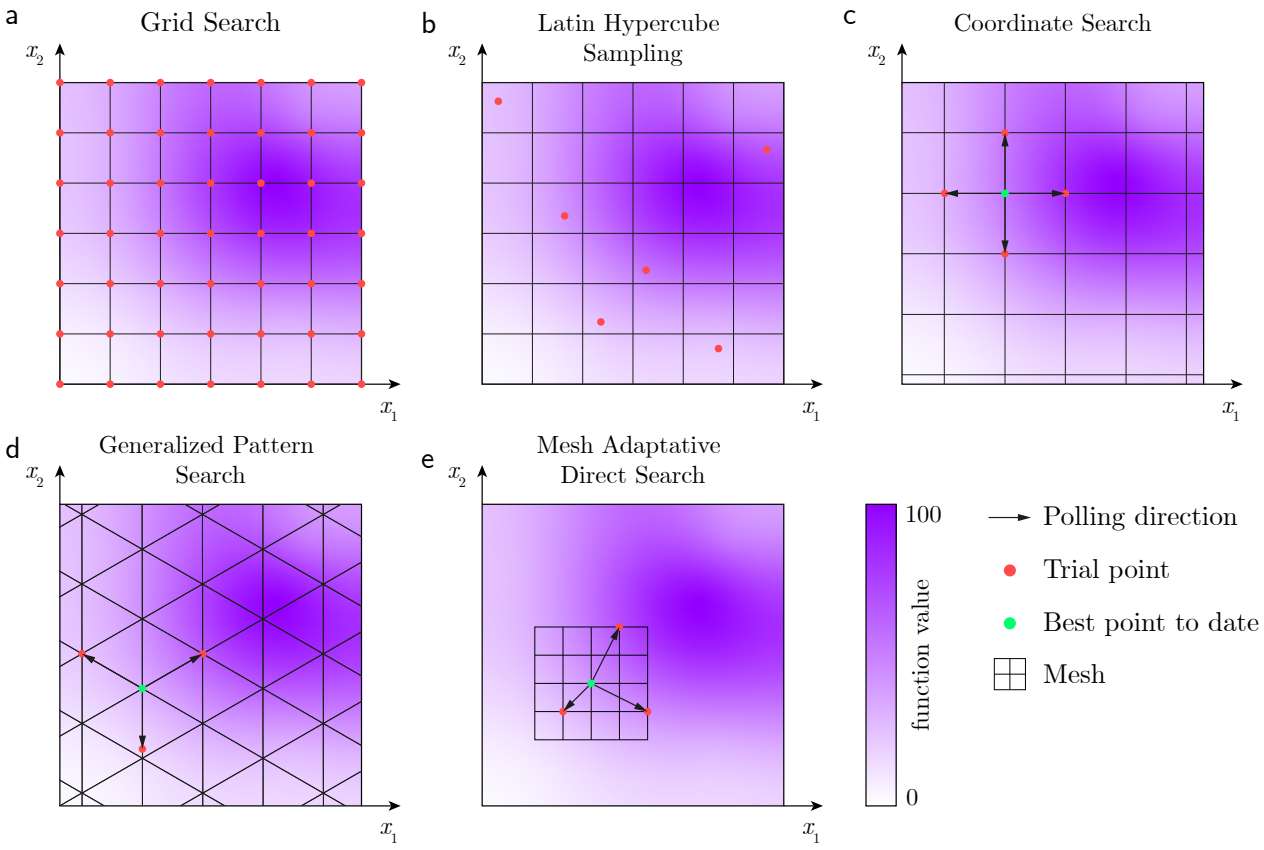

Figure 2.9 **Mesh-based optimization methods a.** Grid Search. **b.** Latin Hypercube Sampling based on the same mesh as the GS [58]. **c.** The polling step of the Coordinate Search algorithm [32]. **d.** Generalized Pattern Search with an equilateral triangular mesh [78]. **e.** A polling step of the Mesh Adaptive Direct Search [4].

Several methods can be used to solve blackbox problems, with mesh-based approaches being one of the most popular:

— **Grid Search (GS)**: Evaluates the design space at points defined by a grid over the area (Figure 2.9a). The solution is chosen based on the best point evaluated on the grid, which depends on the grid's accuracy. There is no guarantee of optimality.

— **Latin Hypercube Sampling (LHS)** [58]: Partitions the design space and assigns probing points randomly on the grid (Figure 2.9b). Every point is computed, but there is no certainty that the result is optimal.

— **Coordinate Search (CS)** [32]: Involves successive polling steps to probe the neighboring area of the best point along orthogonal directions. A full iteration includes $2.n$ evaluations. Where n is the dimension of the problem. If no better point is found,

the probing vectors' length is reduced. Optimization stops after a defined number of evaluations or when the probing length is below a threshold.

— **Generalized Pattern Search (GPS)** [78]: Similar to CS but allows for a more diverse range of polling directions and includes a "search" step between polling steps to identify promising regions in the design space. This search can be local, with quadratic model based on the previous iterations for example, or global, using other heuristic search methods like Nelder-Mead or the VNS algorithm (Variable Neighborhood Search).

— **Mesh Adaptive Direct Search (MADS)** [4]: Improves the polling step by dynamically transforming the grid, allowing for an infinite number of search directions and making MADS very efficient at escaping local minima. It is the only method supported by rigorous convergence analysis.

The last algorithm is implemented in the open-source software NOMAD [8] coded in C++, but a Python package, PyNOMAD, as well as a MATLAB package, are also available. Mathematical constraints can be treated using the extreme barrier method [7], by simply rejecting the infeasible points. But this approach implies a two-phase optimization where the mathematical constraints are treated in an optimization function to first find a feasible point and then optimize the objective function with automatic discarding of points outside the feasible domain. MADS allows for a finer approach, the progressive barrier [5] that takes into account the constraint violation values.

Other heuristic methods like the Nelder-Mead algorithm [65] use simplexes to navigate the design space but may fall into traps that prevent convergence [59]. Despite this, the Nelder-Mead algorithm is often implemented as a default optimization method in FE software.

CHAPTER 3 SUMMARY OF THE LITERATURE REVIEW AND RESEARCH OBJECTIVES

3.1 Summary of the Literature Review

Origami offers a large variety of shapes and structures that can deform and lead to reconfigurability. The domain does not restrict the use of inspiration from origami, as almost any material can be used to manufacture and actuate origami-like objects. Combined with multistability, one can develop self-locking origami-inspired structures with multiple equilibrium states, each serving a different functionality. Previous research displayed promising applications of origami in various fields such as origami robotics, metamaterials, medicine, and aerospace. Multistability relies on deformation and elastic energy to hold structures in place, and if one wants to engineer more efficient structures, one must be considered in the design phase. Researchers have demonstrated that the physics behind origami can be modeled numerically, either with low-cost and reduced accuracy using discrete models or with more continuous models, e.g, FEM, able to capture local stresses and deformations.

To this day, and to the author's best knowledge, few researchers have conducted studies to optimize multistability in mechanical systems. The reaction force has been studied and optimized in the past for a single unit of bistable beam structure [53]. The promising results showed the emergence of bistable behavior due to the tuning of the beams' thickness. In origami, Lee et al. [49] optimized the energy barrier separating two stable states but did not account for the effective loss of performance caused by hinge stiffness and the residual constraints in additional equilibrium states. A more manufacturing-aware methodology must be implemented to address what is currently missing in origami-inspired multistable optimization projects. Coupling derivative-free and black-box optimization techniques with simulation models could be used to tune the numerical model and produce the best possible structure in terms of multistability.

3.2 Research Objectives

Based on the associated literature review, four critical points are identified as the research objectives for this project:

— **Objective 1: Model** bistable origami by implementing crease folding using FEM on the Abaqus software and through the Python script interface.

  - **Sub-objective 1:** Embody compliant regions into the structure to allow folding of the geometry.
  - **Sub-objective 2:** Output the elastic energy response under deployment.

— **Objective 2: Parameterize** the numerical models to obtain a wide range of feasible geometries.

  - **Sub-objective 1:** Select the design variables that determine the shape of creases to vary the rigidity of the folding regions and illustrate their impact on bistable performance.
  - **Sub-objective 2:** Treat the FEM simulation as a black-box function, where a given input vector will define a specific geometry, and after computation, is associated to an objective function with constraints.

— **Objective 3: Optimize** the parameterized FEM model using a black-box optimization method: MADS algorithm on the software NOMAD.

  - **Sub-objective 1:** Analyze the optimization results both in terms of mechanical and mathematical performance.
  - **Sub-objective 2:** Evaluate the impact of manufacturing limits on the optimization boundaries and the optimal value of bistable performance.

— **Objective 4: Validate** experimentally the numerical results.

  - **Sub-objective 1:** Fabricate physical prototypes using 3D printing techniques.
  - **Sub-objective 2:** Measure experimentally the elastic energy landscape of the samples.

CHAPTER 4 RESEARCH ARTICLE 1 : BLACKBOX OPTIMIZATION FOR ORIGAMI-INSPIRED BISTABLE STRUCTURES

The following section is adapted for a research article, written as a result of this Masters' thesis, and submitted to Extreme Mechanics Letters on the 22nd of august 2024.

Luca Pierre Jean Claude Boisneault • Charles Audet • David Mélançon

Abstract

Bistable mechanical systems exhibit two stable configurations where the elastic energy is locally minimized. To realize such systems, origami techniques have been proposed as a versatile platform to design deployable structures with both compact and functional stable states. Conceptually, a bistable origami motif is composed of two-dimensional surfaces connected by one-dimensional fold lines. This leads to stable configurations exhibiting zero-energy local minima. Physically, origami-inspired structures are three-dimensional, comprising facets and hinges fabricated in a distinct stable state where residual stresses are minimized. This leads to the dominance of one stable state over the other. To improve mechanical performance, one can solve the constrained optimization problem of maximizing the bistability of origami structures, defined as the amount of elastic energy required to switch between stable states, while ensuring materials used for the facets and hinges remain within their elastic regime. In this study, the Mesh Adaptive Direct Search (MADS) algorithm, a blackbox optimization technique, is used to solve the constrained optimization problem. The bistable waterbomb-base origami motif is selected as a case-study to present the methodology. The elastic energy of this origami pattern under deployment is calculated via Finite Element simulations which serve as the blackbox in the MADS optimization loop. To validate the results, optimized waterbomb-base geometries are built via Fused Filament Fabrication and their response under loading is characterized experimentally on a Uniaxial Test Machine. Ultimately, our method offers a general framework for optimizing bistability in mechanical systems, presenting opportunities for advancement across various engineering applications.

Keywords : Origami, Multistability, Blackbox optimization, Finite Element Method

4.1 Introduction

Initially an artistic technique of folding paper, origami is now used in engineering to develop deployable systems whose kinematics are embedded directly in the crease pattern [63]. This has led to the design of sub-millimeter scale mechanical metamaterials [41, 42, 54, 86] and robots [51, 70] capable of shape reconfiguration as well as meter scale structures [60, 95, 92] that deploy using simple actuation methods.

In engineering, origami research is mainly divided into two categories: rigid foldable [46, 31, 57] and deformable [56, 37, 38]. Whereas rigid origami can be studied purely from a mechanism point of view, i.e., by solving the equations of motion of rigid bodies [47], deformable origami requires taking into account the storage of elastic energy to predict deployment. Mathematically, the folding of deformable origami structures can either be modeled using simple, discrete elements such as bars along a fold line and torsional springs across it [91], or using more accurate, finite elements such as thin shells [93]. While using the Finite Element Method (FEM) to simulate folding provides a rich description of the stored elastic energy inside the origami structure, it comes with an increase in computational cost.

During deployment, deformable origami structures store elastic energy mostly through folding of the hinges and bending of the facets. While hinging energy is typically monotonic, bending energy can be non-monotonic in some origami patterns, leading to multistability [18]. This property is defined as the coexistence of two or more equilibrium states where the elastic energy is locally minimized. Recent works have shown that these stable configurations can be accessed via an imposed displacement [37, 23], magnetic field [66, 28], internal pressure [60, 61, 88], or through stimuli-responsive materials [29, 89]. Because multistable structures embed self-locking, they offer an advantage over other deployable systems relying on external mechanisms, such as contact [17, 42] and spring-loaded devices [39]. Most of the current multistable origami literature focuses on characterizing the influence of the pattern geometry on multistability [87, 35]. Some works have put forward optimization as a way to increase bistability, but they are limited to simple beam-based structures [53] or only maximize geometrical incompatibility [49, 61]. However, to transition toward engineering applications, manufacturing parameters, such as panel thickness and hinge type, become important.

This work puts forward a general framework to optimize and take into account multistability when designing origami-inspired structures. In Section 4.2, the bistable waterbomb pattern [37] is chosen as a case study and a modeling representation based on compliant crease is presented. Its deployment and the associated bistability performance are computed via FEM and validated on 3D printed samples. The geometry is then parameterized, and the selected

design variables are shown to have an impact on the bistable behavior of the origami structure. The question of finding the best possible geometry is posed as a mathematical optimization problem, in which the objective function consists in maximizing the energy required to switch back from the second to the first state, and is constrained both by the fabrication limitation and the mechanical stress experienced during the deployment phase. Evaluating the objective and constraint functions requires launching a time-consuming FEM simulation, which often fails to compute due to instabilities and nonlinearities in the mathematical formulation. The resulting optimization problem is solved by the Nomad [8] implementation of the Mesh Adaptive Direct Search (Mads) [4] derivative-free constrained blackbox optimization algorithm. A coupled blackbox-FEM framework is developed to optimize the parameterized model, while taking into account the multiple failed evaluations. Finally, in Section 4.3, the optimization process is applied with and without considering manufacturing limits and the resulting geometries are presented.

4.2 Methodology

4.2.1 The origami waterbomb base pattern: a simple bistable structure

The waterbomb base pattern is selected as a case study to describe the methodology developed herein to improve the mechanical performance of bistable origami structures. This choice is motivated by its simple geometry, ease of fabrication, and extensive researches on its kinematics [40], bistability [37], and potential applications to tune acoustic waves [13], create logic gates [79], build mechanical metamaterials [12], and develop innovative origami-based robots [29]. The geometrical description of the waterbomb base is presented in Figure 4.1. The classical approach to obtain the waterbomb fold is by dividing evenly a flat, circular surface with mountain and valley folds around its geometrical center. This axisymmetric pattern usually involves $n = 4$ repetitions so that opposite folds are of the same type, mountain or valley, making the structure easier to fold in a cone-like shape of height h (see Figure 4.1a). When the central node, i.e., the tip of the cone, is pulled down by a distance δ, the structure starts deforming elastically through the bending of the triangular faces and stretching of the fold lines. When $\delta = h$, this stored elastic energy U reaches a maximum. Passed this point, i.e., for $\delta > h$, the energy U decreases towards a second local minimum. If the hinges connecting the panels are ideal pivot connections, this second stable state is z-symmetrical to the initial configuration so that there is no bending of the triangular faces. The bistable behavior of the waterbomb pattern can be characterized mechanically by plotting U as a function of δ, as shown in Figure 4.1b. For the case where there is no energy cost associated with rotating the faces along a fold line, face bending prevails and the energy curve shows

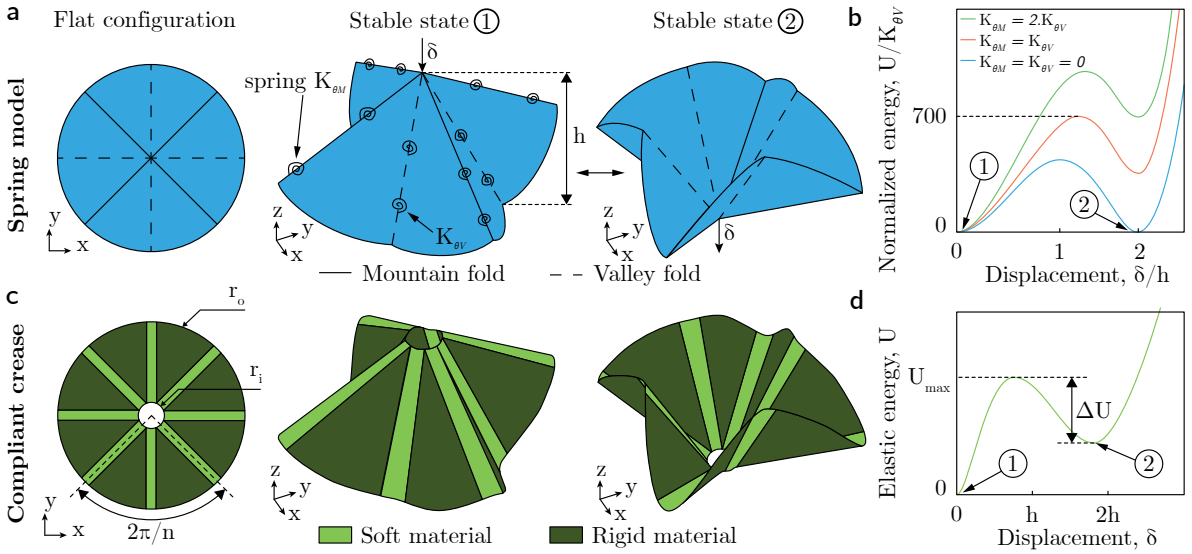

Figure 4.1 **Modeling the four-fold waterbomb origami pattern with different levels of complexity. a.** Simplified representation of the waterbomb with fold lines modeled as torsion springs shown in the flat configuration as well as in both stable states. **b.** Energy-displacement curve of the spring model and the effect of increasing the hinging energy by adding springs of stiffness $K_{\theta M}$ and $K_{\theta V}$ at the mountain and valley folds, respectively. **c.** Compliant crease representation of the waterbomb with the fold lines modeled as regions of soft material shown in the flat configuration as well as in both stable states. **d.** Energy-displacement curve of the compliant crease model.

two stable states with zero energy. Instead, if torsion springs of stiffness K_θ are added to model the hinging energy, the second equilibrium state has residual stresses, resulting in a nonzero energy local minimum. Hanna *et al.* [37] have shown that a different stiffness in the mountain and the valley hinges, i.e., $K_{\theta M}$ and $K_{\theta V}$, respectively, will affect the amount of energy required to switch back from the second state to the first one. In Figure 4.1b, their results are reproduced numerically for three different scenarios, i.e., $K_{\theta M} = K_{\theta V} = 0$ (blue curve), $K_{\theta M} = K_{\theta V}$, with $K_{\theta V} \neq 0$ (red curve), and $K_{\theta M} = 2K_{\theta V}$, with $K_{\theta V} \neq 0$ (green curve).

In the most simplified representation of the waterbomb pattern, mountain and valley folds are modeled as spring-loaded hinges that connect flat panels. A more continuous way of modeling this origami pattern is to represent the folding geometry using compliant creases [93]. In this technique, fold lines are substituted with wider and softer regions to allow rotation and the central node is replaced by a hole (see Figure 4.1c where the dark and light shades correspond to faces and compliant creases, respectively). This allows to take the hinge width into account, and a higher-order of geometric continuity is implemented, i.e., smooth folds [69] between the faces. Applying the compliant crease origami modeling produces the

same downside effect as adding torsion springs on the simplified model : the second stable state has nonzero elastic energy. This type of bistable energy curve has two characteristic features: a local maximum of elastic energy between the two stable states, $U_{\max}$, and an energy well depth of the second stable state, ΔU (see Figure 4.1d). Here, their ratio is used to quantify the bistability, ϕ, of the structure:

$$\phi = \frac{\Delta U}{U_{\max}}. \tag{4.1}$$

When $\phi \to 0$ the structure becomes marginally bistable. Instead, when $\phi = 1$, the two stable states have the same amount of stored elastic energy.

4.2.2 Simulating bistable origami via the Finite Element Method

In this work, FEM is used to compute the bistability, ϕ, of the compliant crease waterbomb. The origami pattern is discretized with four-node, linear shell elements (element code S4 in Abaqus Standard 2022) with linear elastic material model with elastic moduli E_f, E_c, Poisson's ratios, ν_f, ν_c, densities, ρ_f, ρ_c, and elastic limit, S_Y^f, S_Y^c for the faces and compliant creases, respectively. As shown in Figure 4.2a, for given face and crease materials, five design variables are selected to generate a wide range of geometry for the waterbomb model: three angles, $\boldsymbol{\theta_i}$, with $\boldsymbol{i \in \{1, 2, 3\}}$, shaping the compliant crease, $\boldsymbol{\omega = t_c/t_f}$, the ratio of out-of-plane crease thickness over face thickness, and $\boldsymbol{h/r_o}$, the height of the waterbomb in its first stable state normalized by the outer radius. Together, these values constitute the input vector $\boldsymbol{x = (\theta_1/\alpha, \theta_2/\alpha, \theta_3/\alpha, \omega, h/r_o) \in \mathbb{R}^5}$, with $\boldsymbol{\alpha = \pi/n}$. The inner radius, $\boldsymbol{r_i/r_o = 1/6}$, and the number of cyclic symmetry, $\boldsymbol{n = 4}$, are fixed to reduce the dimensionality of the design space. To speed up the computation, only $\boldsymbol{1/2n}$ of the complete pattern is modeled and cyclic boundary conditions are applied on the outer edges. In a cylindrical framework, this means to the two lateral edges cannot move along the $\boldsymbol{\theta}$-axis, as well as rotate around the $\boldsymbol{r}$-axis and the $\boldsymbol{z}$-axis. The FEM simulation is divided into two steps (see Figure 4.2b):

— **Step-1: Forming.** The waterbomb pattern is deformed from the flat configuration to the deployed state defined by $\boldsymbol{h/r_o}$. To do so, the nodes located on the inner hole are pulled up by a distance $\boldsymbol{\delta_1 = h}$, and the node defined by $\boldsymbol{\theta_2}$, i.e., the node located at the frontier between the face and the crease, is fixed with respect to the $\boldsymbol{z}$-axis. The geometry obtained at the end of this step is retrieved and taken without any mechanical stress as the base geometry for the second step.

— **Step-2: Actuation.** The waterbomb pattern is actuated from the first to the second stable state. To do so, the nodes on the inner hole are pulled down by a distance

$\boldsymbol{\delta_2 = 2h}$, while the node defined by $\boldsymbol{\theta_3}$, is locked relative to the $\boldsymbol{z}$ translation,

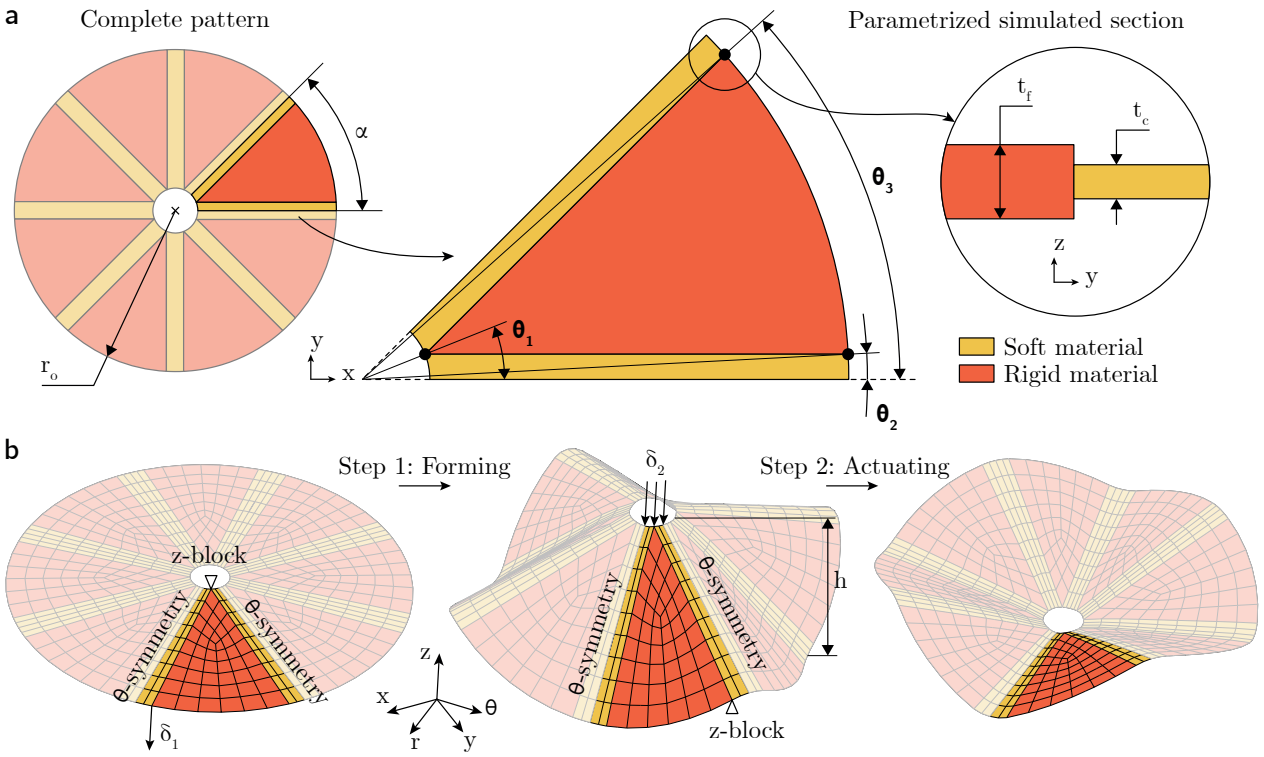

Figure 4.2 **Parametrized FEM of the waterbomb origami pattern. a.** Representation of the geometrical variables $\boldsymbol{\theta_1}$, $\boldsymbol{\theta_2}$, $\boldsymbol{\theta_3}$, $\boldsymbol{\omega = t_c/t_f}$, and $\boldsymbol{h/r_o}$ on the simulated part of the structure. **b.** Meshed model of the waterbomb at the beginning and the end of the **Forming** and the **Actuation** steps as well as the associated boundary conditions imposed.

During the FEM simulation, the stored elastic energy is obtained by integrating the reaction force with respect to the applied displacement on the nodes of the inner holes during the **Actuation** step. In addition, the maximum von Mises stress developed in the structure, $\boldsymbol{\sigma_{max}}$, as well as its location and associated displacement $\boldsymbol{\delta}$ are extracted from the FEM simulation to ensure the materials remain in their elastic regime, i.e., $\boldsymbol{\sigma_{max} < S_Y^i}$, with $\boldsymbol{i \in \{f, c\}}$ if the $\boldsymbol{\sigma_{max}}$ is developed in the faces or crease, respectively.

To highlight the effect of the geometrical parameters on the bistability of the waterbomb motif, the FEM simulation is conducted on three different patterns:

— **Design I** with $\boldsymbol{x_I = \left(\theta_1^I/\alpha, \theta_2^I/\alpha, \theta_3^I/\alpha, \omega^I, h^I/r_o\right) = (0.1, 0.5, 0.9, 1.0, 0.6)}$,

— **Design II** with $\boldsymbol{x_{II} = (0.5, 0.6, 0.7, 0.5, 0.704)}$,

— **Design III** with $\boldsymbol{x_{III} = (0.31, 0.46, 0.9, 1.5, 0.374)}$.

These input vectors are chosen to represent the wide range of feasible geometries. **Design I** is the standard waterbomb with parallel creases and equal thickness between facets and creases. Differently, **Design II** includes creases wider, but thinner than facets. Finally, **Design III** alternates narrow and wide creases which are thicker than the facets. For each design, the top and front views as well as the two stable configurations and the von Mises stress field in the second stable state are shown in Figure 4.3a.

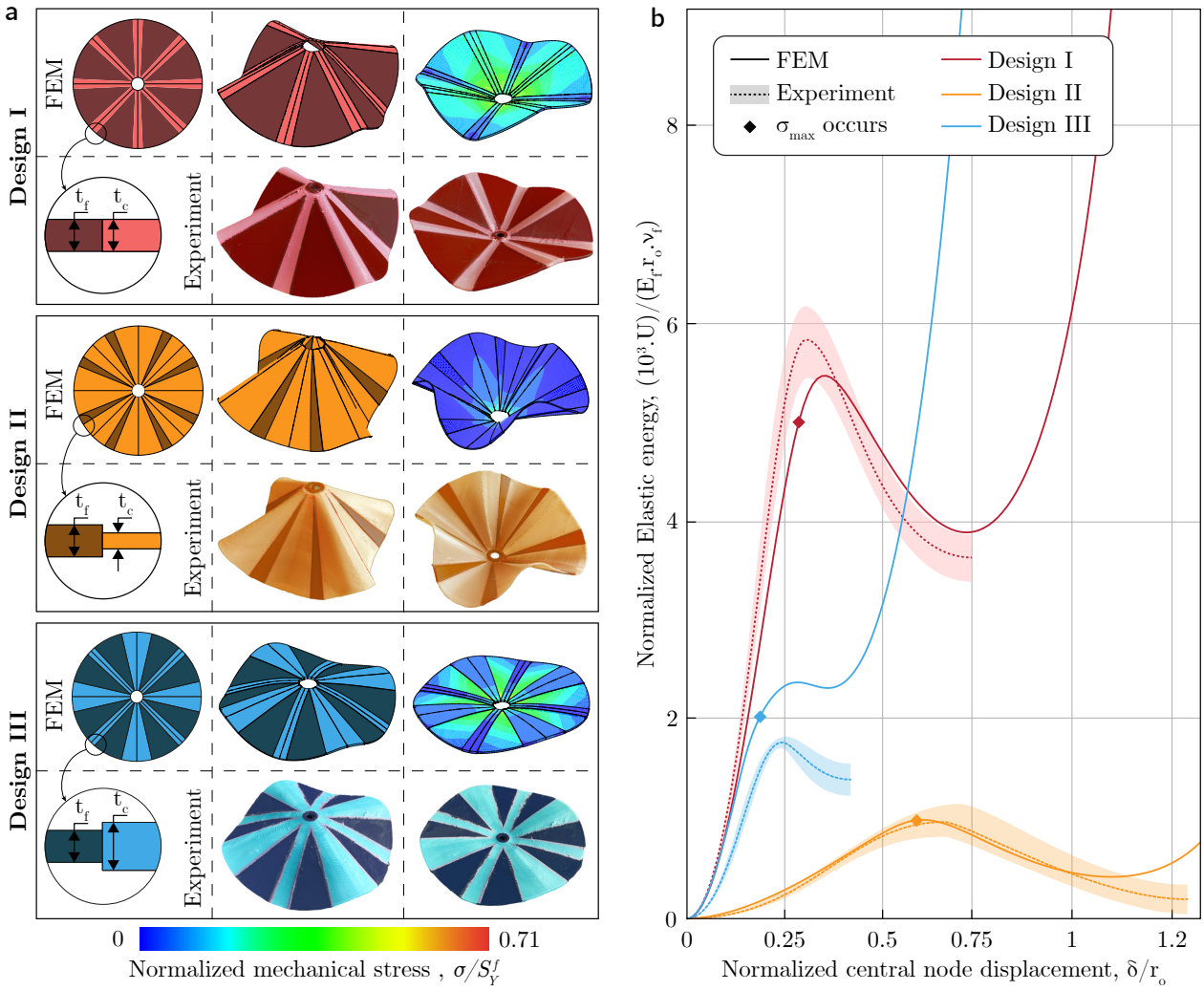

Figure 4.3 **Impact of the design variables on the bistability performance of the waterbomb pattern. a.** The three designs obtained through the parametrization and their geometrical representation in both equilibrium states for the FEM and the 3D printed models. **b.** Evolution of the elastic energy during deployment for the three designs showing the comparison between FEM simulations and experimental tests.

Here, the ratios $\boldsymbol{E_f/E_c = 21.67}$ and $\boldsymbol{\nu_f/\nu_c = 0.78}$ are considered in the numerical simulations. The evolution of the elastic energy during the deployment of each design is

presented in Figure 4.3b and reveals that changes in the size and shape of the compliant creases can affect drastically the bistable performance of the waterbomb pattern. The elastic energy is normalized with respect with the outer radius $\boldsymbol{r_o}$ of the pattern, as well as the facet's material properties $\boldsymbol{E_f}$ and $\boldsymbol{\nu_f}$. For **Design I**, the bistable performance is characterized by $\boldsymbol{\phi^I = 28.85\%}$, with $\boldsymbol{\Delta U^I/(E_f r_o \nu_f) = 1.56 \times 10^{-3}}$ and $\boldsymbol{U^I_{max}/(E_f r_o \nu_f) = 5.41 \times 10^{-3}}$. **Design II** exhibits an increase of bistable performance with $\boldsymbol{\phi^{II} = 57.74\%}$, $\boldsymbol{\Delta U^{II}/(E_f r_o \nu_f) = 0.57 \times 10^{-3}}$, and $\boldsymbol{U^{II}_{max}/(E_f r_o \nu_f) = 0.98 \times 10^{-3}}$. Finally, **Design III** displays marginal bistability with $\boldsymbol{\phi^{III} = 2.4\%}$, $\boldsymbol{\Delta U^{III}/(E_f r_o \nu_f) = 0.05 \times 10^{-3}}$, and $\boldsymbol{U^{III}_{max}/(E_f r_o \nu_f) = 2.36 \times 10^{-3}}$. Note that the geometry of the creases affect not only the multistability ratio $\boldsymbol{\phi}$, but also the maximum elastic energy $\boldsymbol{U_{max}}$, the barrier of energy in the second stable state $\boldsymbol{\Delta U}$, and the displacement $\boldsymbol{\delta}$ required to switch to the second stable state.

Additionally, for the three design, the maximum mechanical stress is developed right before the local maximum of energy (see diamond markers in Figure 4.3b) and is located near the hole and on the stiff faces. This maximal value, normalized by the elastic limit of the facets material, is $\boldsymbol{\sigma^I_{max}/S^f_Y = 0.708}$, $\boldsymbol{\sigma^{II}_{max}/S^f_Y = 0.685}$ and $\boldsymbol{\sigma^{III}_{max}/S^f_Y = 0.473}$ for the three designs. The location of the maximum stress for the second stable state stays the same (see the contour maps in Fig.4.3a), but one notes that a higher mechanical stress is associated with a lower bistability performance : $\boldsymbol{\sigma^I_{state2}/S^f_Y = 0.304}$, $\boldsymbol{\sigma^{II}_{state2}/S^f_Y = 0.266}$ and $\boldsymbol{\sigma^{III}_{state2}/S^f_Y = 0.432}$.

4.2.3 Experimental validation

To validate the FEM simulations, physical prototypes of **Designs I-III** are fabricated using the Fused Filament Fabrication (FFF) method. FFF enables fast prototyping of multi-material origami patterns [85]. Here, the crease regions are printed with thermoplastic polyurethane (TPU from Eryone with $\boldsymbol{E_c = 120}$ MPa, $\boldsymbol{\nu_c = 0.45}$, $\boldsymbol{\rho_c = 1200}$ kg/m^3 and $\boldsymbol{S^c_Y = 50}$ MPa) and the faces with polylactic acid (PLA from Raise3D with $\boldsymbol{E_f = 2600}$ MPa, $\boldsymbol{\nu_f = 0.35}$, $\boldsymbol{\rho_f = 1040}$ kg/m^3 and $\boldsymbol{S^f_Y = 50}$ MPa). Using the initial deformed shape obtained from the FEM simulation of the waterbomb (**Step-1: Forming**), a CAD model is generated. Interlocking geometry are added to improve bonding between the soft and the rigid regions [44]. This way, when the model is sliced, the interface between faces and creases will be composed of layers of an alternating set of PLA and TPU layers (see the Supplementary Materials section S1 for additional details on the fabrication of the physical prototypes).

To experimentally measure the stored elastic energy during folding, the physical prototypes

are tested on a uniaxial test machine (MTS Insight Electromechanical 50), fitted with a **100** N load cell. Inspired by previous experimental work on the waterbomb pattern [37], each specimen is placed on custom-build supports that emulate the same conditions as the numerical simulation, i.e., it is installed on triangular guiding rails preventing it from rotating around the $\boldsymbol{z}$-axis, and the central hole is attached to the load cell through a fixed bolt to measure the reaction force during the deployment (see the Supplementary Materials S2 for additional details on the experimental testing). The crosshead imposes a vertical displacement of $\boldsymbol{\delta_{exp}}$ at a rate of **0.05** mm/s, to create quasi-static conditions, until the second stable state is reached. After the test, the reaction force $\boldsymbol{F_{\mathbf{exp}}}$ is integrated along the displacement to obtain the experimental elastic energy $\boldsymbol{U_{\mathbf{exp}}}$ of the waterbomb prototype:

$$\boldsymbol{U_{\mathbf{exp}}(\delta_{exp})} = \int_{\mathbf{0}}^{\boldsymbol{\delta_{exp}}} \boldsymbol{F_{\mathbf{exp}}(\delta)}\, \mathrm{d}\boldsymbol{\delta}. \tag{4.2}$$

In Figure 4.3a, representative specimens of each prototype are shown in both stable states, and their measured energy-displacement curves are plotted as doted line in Figure 4.3b with the standard deviation from five tests specimens shown as shaded areas. From the comparison with the simulated model, one can assess that the deformed shapes obtained with the 3D printed sample match qualitatively the computation both in the first and the second stable states (see Figure 4.3a). Quantitatively, **Design I** shows the closest match between predicted and measured energy landscapes with a relative error of $\boldsymbol{\epsilon^{I}_{U_{\max}} = 5.5\%}$ on the maximal amount of energy $\boldsymbol{U_{\max}}$ and an error on the displacement of the central node in the second stable state $\boldsymbol{\epsilon^{I}_{\delta/r_o} = 4.1\%}$. **Design II** also shows good agreement between simulations and experiments with $\boldsymbol{\epsilon^{II}_{U_{\max}} = 2.9\%}$ and $\boldsymbol{\epsilon^{II}_{\delta/r_o} = 18.4\%}$. However, there are discrepancies between the predicted and measured energy landscapes for **Design III** with $\boldsymbol{\epsilon^{III}_{\delta/r_o} = 15.9\%}$ and $\boldsymbol{\epsilon^{III}_{U_{\max}} = 25.7\%}$. This deviation could be attributed to the boundary condition imposed during the testing phase which can slightly differ from the one set numerically. In fact, the larger soft creases of **Design III** close to the hole where the screw is fixed for mechanical testing could add additional compliance that is not modeled in the FEM simulations.

4.2.4 Optimizing the mechanical performance of bistable origami

Optimization algorithms can be used to tune the geometrical parameters of the waterbomb origami with compliant creases in order to address the loss of bistable performance seen in Figure 4.3b. Consider a simulation that takes an input vector $\boldsymbol{x}$ containing the five design variables, and outputs the bistable performance of the associated structure, $\boldsymbol{\phi}$, as well as the maximum von Mises stress experienced by the structure, $\boldsymbol{\sigma_{\max}}$. The input vector $\boldsymbol{x} \in \mathbb{R}^{\mathbf{5}}$ is bounded by the two vectors $\boldsymbol{l_b}$ and $\boldsymbol{u_b}$, respectively the lower and the upper boundaries.

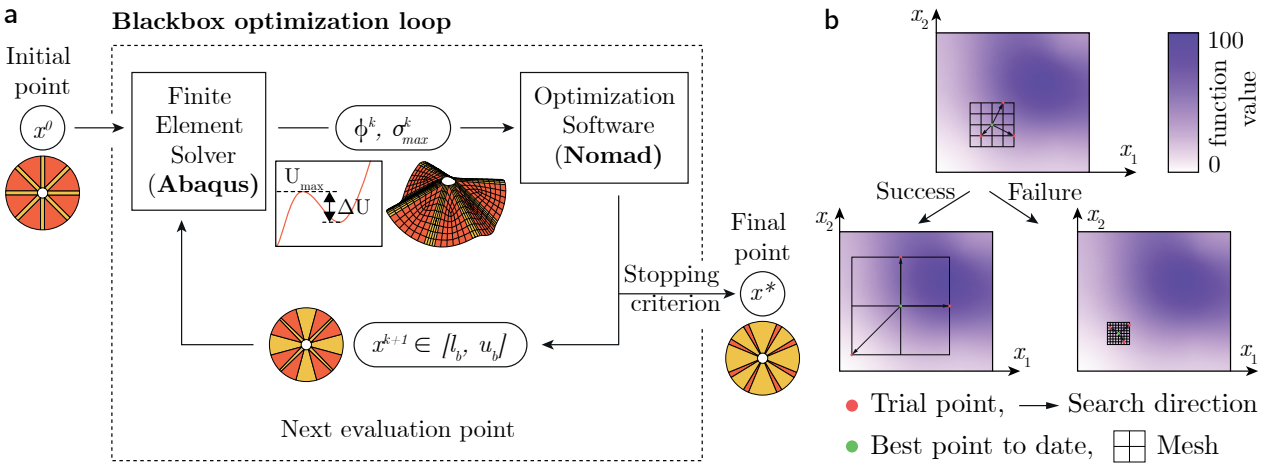

Figure 4.4 **Strategy to optimize the bistability of origami-inspired structures. a.** Coupling of the FEM blackbox with the optimization algorithm NOMAD. **b.** Successive polling steps on an arbitrary 2D function with MADS depending if the previous iteration was a success or a failure.

This ensures that the optimization will not diverge and deliver unrealistic results. To avoid mechanical failure, the maximum stress experienced by the structure $\boldsymbol{\sigma_{max}}$ must not exceed the yield strength, $\boldsymbol{S_Y}$, of the material. The corresponding constrained optimization problem is then formulated as :

$$\begin{aligned} \max_{\boldsymbol{x}\in\mathbb{R}^5} \quad & \phi = \frac{\boldsymbol{\Delta U}}{\boldsymbol{U_{max}}} \\ \text{s.t.} \quad & \boldsymbol{\sigma_{max}} \leq \boldsymbol{S_Y} \\ & \boldsymbol{l_b} \leq \boldsymbol{x} \leq \boldsymbol{u_b}. \end{aligned} \tag{4.3}$$

This optimization problem may be regarded as a blackbox : at each iteration $\boldsymbol{k}$ only the input $\boldsymbol{x_k}$ and output $\boldsymbol{\phi^k}$ and $\boldsymbol{\sigma^k_{max}}$ data are known, and the time-consuming FEM simulations are considered hidden. In the present case, derivatives are difficult to obtain due to the numerous fails in the computation, therefore derivative-free optimization techniques [7] are required.

The NOMAD blackbox optimization software, which implements the MADS algorithm [4], is chosen to maximize the objective function while taking into account the constraints of the problem. Thanks to the dynamic adaption of the size of the searching space between each iteration, MADS allows an efficient exploration of the design space. Additionally, NOMAD has proven successful in the case of blackbox with a long computational time [10] and with large part of the design space covered by hidden constraints, i.e., sets of points that cannot be computed or that do not output numerical values when fed to the blackbox [20]. Numerous studies in fields such as biomedical, aerospace or electrical engineering, have successfully used NOMAD to solve optimization problems [1]. This software is also provided with a python

package, PyNOMAD, allowing easy communication with the FE software.

In the present problem, each call to the blackbox requires an average of **110** seconds to compute when successful, and computation fails on **30**% of the calls, which makes NOMAD a suitable solution to solve the problem. Computations are made on an Intel Core i9-9900K processor. Here, every evaluation requires a different computation time, depending on how well the FE solver performs on the model defined by a given input vector. The optimization process is initiated with **Design I**, a geometry with parallel creases and uniform thickness across the structure. This geometry is set in NOMAD as the initial point $\boldsymbol{x^0} = \left(\boldsymbol{\theta_1^0/\alpha, \theta_2^0/\alpha, \theta_3^0/\alpha, \mu^0, h^0/r_o}\right) = \boldsymbol{(0.1, 0.5, 0.9, 1.0, 0.6)}$, and is known to provide a bistable performance of $\boldsymbol{\phi^I = 28.85\%}$. NOMAD sends these parameters to the blackbox for the first evaluation and the FE software, which computes the stored elastic energy and von Mises stress during folding, outputs back to NOMAD both the bistable performance $\boldsymbol{\phi}$ as well as the maximum value of stress $\boldsymbol{\sigma_{max}}$ (Figure 4.4a). The next evaluation points are determined by selecting $\boldsymbol{N+1}$ random points (with $\boldsymbol{N}$ is the dimension of the design space) on a grid centered on the best evaluation yet. A complete iteration of the optimization algorithm consists of the evaluation of these $\boldsymbol{N+1}$ points. If the multistable performance $\boldsymbol{\phi}$ of the evaluation $\boldsymbol{k}$ is better than any of the previous best evaluations, $\boldsymbol{x^k}$ and the corresponding $\boldsymbol{\phi^k}$ become the new champion and the size of the grid that determines the next iteration points is expanded. However, if the computation does not result in an improvement of the objective function, the size of the grid is reduced for the next iteration. If the mechanical stress exceeds the yield stress limit, the point is discarded and cannot be the final output value of the optimization, i.e., it is considered a failed evaluation. The algorithm continues until it reaches a maximum of **1000** evaluations. The optimization process is schematized in Figure 4.4b.

4.3 Optimization results

The optimization is launched considering manufacturing limits, i.e., ensuring a minimum hinge width of **0.4** mm, the diameter of the nozzle used for 3D printing the samples. The associated mathematical lower and upper boundaries $\boldsymbol{l_b}$ and $\boldsymbol{u_b}$ as well as the evolution of the bistable performance $\boldsymbol{\phi(x)}$ with the number of evaluations are displayed in Figure 4.5a. The design variables of the optimize geometry are $\boldsymbol{x^a} = \left(\boldsymbol{\theta_1^a/\alpha, \theta_2^a/\alpha, \theta_3^a/\alpha, \omega^a, h^a/r_o}\right) = \boldsymbol{(0.1000, 0.1000, 0.5421, 0.5296, 0.7359)}$ with an associated bistable performance of $\boldsymbol{\phi_a = 64.8\%}$. The performance here is more than doubled if compared from the initial design (see the energy landscape and stable configurations of the initial and optimized geometries in Figs. 4.5f-g). Around **30%** of the evaluations performed ended up failing. This result can be

linked to the increase of the last variable, $\boldsymbol{h/r_o}$. Tall and narrow waterbomb folds are associated with high geometrical frustration during reconfiguration and this can introduce high nonlinearities in the numerical simulations. To reduce the number of failed evaluations, a second optimization is launched with the initial height fixed to $\boldsymbol{h/r_o = 0.6}$ along the process. This optimization produces the final vector $\boldsymbol{x^b = (0.4366, 0.9000, 0.9000, 0.5000, 0.6000)}$ and the bistable performance $\boldsymbol{\phi_b = 58.4\%}$ as shown in the convergence plot of Figure 4.5b. While this represents a loss of $\mathbf{6.4\%}$ compared to the results in Figure 4.5a, it still shows a two-fold increase with respect to the initial design. In addition, the number of failed computations goes from $\mathbf{30\%}$ to only $\mathbf{1\%}$ over $\mathbf{1000}$ evaluations. For the two different optimizations, the convergence is fast with $\mathbf{99\%}$ of the final performance already reached after only $\mathbf{25}$ evaluations.

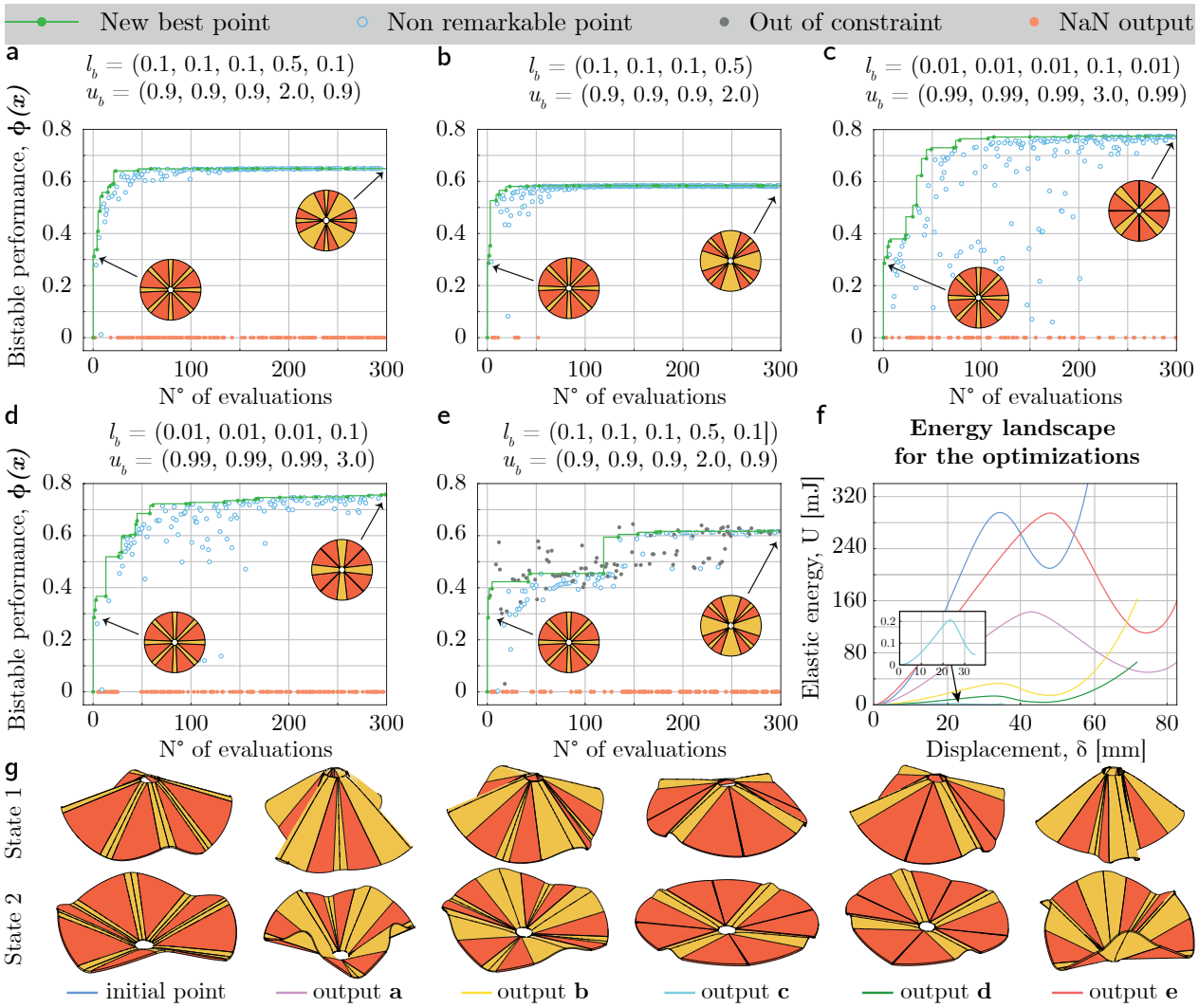

Figure 4.5 **Results of the blackbox optimization.** Bistable performance $\boldsymbol{\phi(x)}$ as a function of the number of evaluations when taking into account manufacturing limits while leaving free **(a)** and fixing **(b)** the initial height $\boldsymbol{h/r_o}$. Effect of increasing the range of the design variables on $\boldsymbol{\phi(x)}$ while leaving free **(c)** and fixing **(d)** the initial height $\boldsymbol{h/r_o}$. **e.** Effect of adding an additional constraint on the maximum energy developed during deployment $\boldsymbol{U_{max}}$. **f.** Evolution of the elastic energy during deployment for the initial geometry and the five optimized geometries **(a)**-**(e)**. **g.** The two stable states of the waterbomb for the initial geometry and the five optimized geometries.

From the insets showing the final geometries in Figs. 4.5a-b and the stable states in Figure 4.5g, one notes that the optimization leads to configurations which reach the mathematical constraints for certain angles $\boldsymbol{\theta_i/\alpha}$, i.e., narrow compliant creases. To investigate the potential gain associated with a manufacturing technique with higher resolution, the lower/upper boundaries on $\boldsymbol{\theta_i/\alpha}$ are decreased/increased and two additional optimizations are launched:

one with all five design variables (Figure 4.5c) and one with the initial height fixed to **0.6** (Figure 4.5d). For both cases, the valley folds of the final geometry become even narrower to increase the bistable performance to $\boldsymbol{\phi_c = 77.7\%}$ and $\boldsymbol{\phi_d = 76.8\%}$ (see the corresponding convergence graphs in Figs. 4.5c-d, energy curves in Figure 4.5f, and stable configurations in Figure 4.5g). Importantly, for these two cases, the increase in bistability performance is linked to steep lowering in the elastic energy. While for the initial design $\boldsymbol{U^0_{max} = 36.93}$ **mJ**, the two optimal geometries shown in Figs. 4.5c-d display $\boldsymbol{U^c_{max} = 0.21}$ **mJ** and $\boldsymbol{U^d_{max} = 1.57}$ **mJ**, respectively. For load-bearing applications, one may want to design bistable origami structures which maximize bistability while being able to develop a high amount of elastic energy during deployment. To do so, two methods can be applied : using stiffer materials to manufacture the structure or adding $\boldsymbol{U_{max}}$ a new mathematical constraint in the optimization. Here, the second approach is implemented with the added constraint forcing the optimization to seek for designs with at least the same $\boldsymbol{U_{max}}$ as the initial design :

$$\boldsymbol{U_{max} \geq U^0_{max}} \tag{4.4}$$

In Figure 4.5e, the last case is presented leading to $\boldsymbol{x^e = (0.4425, 0.8921, 0.8999, 0.6976, 0.8690)}$ with a bistable performance of $\boldsymbol{\phi_e = 62.3\%}$. For this last scenario, the convergence of the optimization displays two successive plateaus, caused by the additional difficulty for the algorithm to find geometries that sustain an acceptable level of maximum elastic energy. The output geometry is almost identical to the one obtained in Figs 4.5a-b, but with a higher initial height and thicker soft regions, characteristics that affect the order of magnitude of the elastic energy response.

4.4 Discussion

In this work, an optimization framework is developed to improve the bistability performance of origami-inspired structures and applied to the waterbomb base pattern. The optimization results highlight a two-fold increase in bistability performance from the classic straight crease waterbomb pattern to a more complex geometry with uneven creases. The methodology developed here is general and can be applied to other bistable origami-inspired structures (see the Supplementary Materials section S3 for more details).

The presented framework is adaptable and could be further improved. First, implementing a bar-and-hinge model [90] as surrogate computation model [14, 9] could speed up the optimization. Additional variables could be easily introduced in the algorithm, e.g., a categorical variable [6] that would determine the material used for each region of the origami pattern,

or curved creases [33] to get more flexibility on the crease shape. As shown with the optimization results in Figure 4.5c-d, relaxing the optimization bounds, which could be possible with other, high resolution fabrication techniques such as composite laminate [75], could further increase bistability. Finally, the optimization strategy could be extended to multistable origami structures, i.e., with more than two stable states. To do so, one could use multi-objective optimization, but this technique tends to lack efficiency and often designers have to prioritize one objective over the other [11]. As multistable origami structures are often made of an assembly of building blocks, e.g., kresling arrays [81], the optimization could be carried both locally on individual components and globally to ensure geometric compatibility.

Acknowledgments

Funding: This work was funded by Audet's NSERC Canada Discovery Grant 2020–04448 and by Melancon's research start-up grant from Polytechnique Montréal. **Author contributions:** L.B., C.A., and D.M. proposed and developed the research idea. L.B. performed the FEM simulations, fabricated the physical prototypes, and developed and ran the blackbox optimization. L.B., C.A. and D.M. wrote the paper. C.A. and D.M. supervised the research. **Competing interests:** The authors declare no conflict of interest. **Data and materials availability:** The data that support the findings of this study are available on request from the corresponding author. The optimization code described schematically in Figure 4.4 is available on Github at `https://github.com/lm2-poly/OriMads`

CHAPTER 5 SUPPLEMENTARY INFORMATION FOR THE ARTICLE

5.1 Fabrication of the waterbomb pattern

Each sample of the waterbomb is fabricated using Fused Filament Fabrication (FFF). The steps to obtained the physical prototypes presented in the main article are presented in Figure 5.1 and listed below.

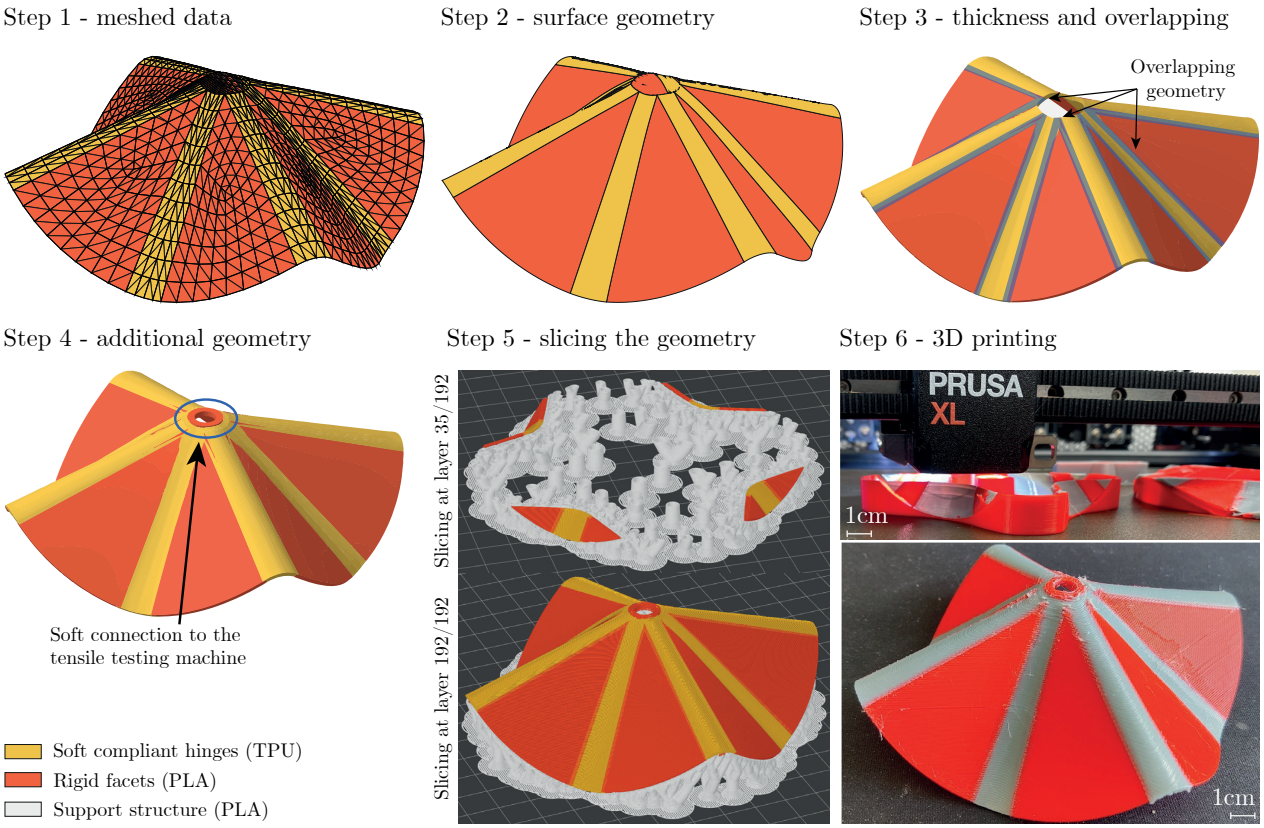

Figure 5.1 **Fabrication of the waterbomb origami pattern from the FEM data to FFF multimaterial 3D printing**

— Step 1: Retrieve the meshed geometry of the initial shape of the **actuation** phase described in Figure 2 of the main article.

— Step 2: Convert the mesh data to a smooth surface using the *Geometry Edit* feature of Abaqus. Export the edited model as a `.step` file.

— Step 3: Import the `.step` file into a CAD software (Catia). Assign surface thickness and an overlapping geometry of **1** mm width each intersection of the facets and the compliant crease

to ensure the interlacing of material when 3D printing. This additional geometry ensures proper bonding between both the rigid and the soft regions.

— Step 4: Fill the inner hole with soft material as well as a stiffer platform for assembly with the tensile testing machine.

— Step 5: Slice the geometry using the software PrusaSlicer. The supports are generated automatically.

— Step 6: Print samples on a PrusaXL using two of the five printing heads available. Note that the three additional heads could be used to implement more materials in the origami geometry. PLA from the supplier Raise3D and TPU from Eryone were used to print the facets and the creases, respectively.

5.2 Mechanical testing of the waterbomb pattern

Inspired by the methodology employed by Hanna et al. [37], the waterbomb origami pattern is tested under punctual loading on a uniaxial tensile testing machine. Because of its bistable behavior, the force will eventually switch direction, i.e., the sample will not lay on the test bench anymore and no value of reaction force will be measured.

For this reason, one needs to measure both responses independently: from state 1 to state 2 (direction a), and separately from state 2 to state 1 (direction b). In direction a, the mountain hinges of the waterbomb rest on triangular rails (Figure 5.2a). In a second phase, the waterbomb is flipped, and the same mountain folds now rest on flat surfaces as shown in Figure 5.2b. The sample is connected to a **100**N load cell via a standard M6 screw (see Figure 5.2c). Both sides are tested and, as expected, direction b displays a reaction force response three times lower than direction a in the first graph of Figure 5.2d. This is due to the residual stress: less energy is required to switch back to the first state. The complete energy curve is constructed as an assembly of the two energy responses. Direction b is placed at the end of direction a as displayed in the second curve of Figure 5.2d. The energy curve is then extracted as the work of the force across the displacement of the central node.

5.3 Additional optimization results

5.3.1 Bistable Origami Star parameterization and optimization

The optimization process developed in the article is applied to a bistable origami star to demonstrate the efficiency of the method on other origami structures. This basic origami shape has been used as a building block to create meter scale functional structures such as arches and shelters [61]. Compared to the waterbomb pattern with two non-flat stable states, the bistable origami star

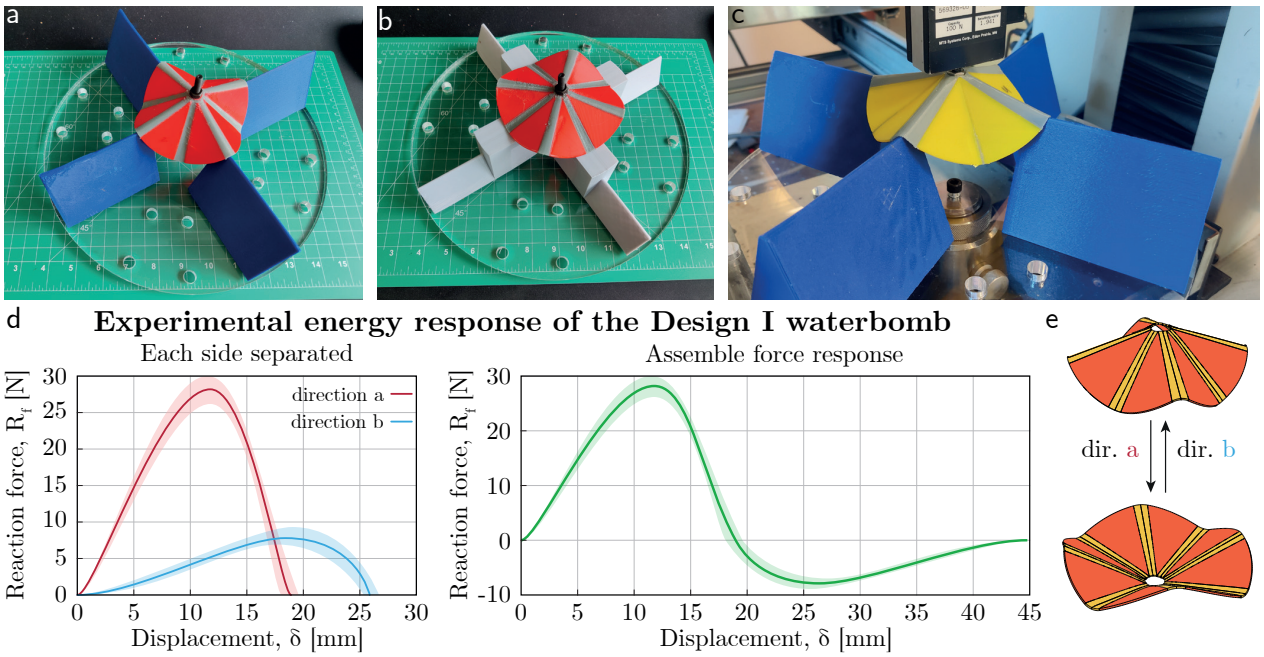

Figure 5.2 **Experimental testing of the waterbomb pattern : a.** Testing setup in direction a, from the first to the second stable state, with the attachment bolt on. **b.** Experimental setup of the waterbomb to switch from the second to the first state (direction b). **c.** Waterbomb fitted in the tensile testing machine. **d.** Representative force-displacement curves recorded during the loading in the two directions and total assembled force-displacement of the waterbomb structure. Shaded areas represent the standard deviation from multiple samples tested. **e.** Schematics of the waterbomb in the two stable configurations along with the directions of switching.

exhibits both a flat and a deployed stable configuration (see Figure 5.3a). Its energy response under deployment can be calculated using FEM (Figure 5.1b), by modeling only $\mathbf{1/(4n)}$ of the structure, where $\boldsymbol{n} = \mathbf{4}$, the number of branches. This can be done as the star pattern is based on three planar symmetries: one vertical ($\boldsymbol{xy}$-plane) and two cyclic symmetries ($\boldsymbol{z\theta}$-plane) on both sides. A vertical displacement is imposed on the rigid facet at the node that is closest to the center of the star. The boundary conditions are displayed in Figure 5.3c.

This origami structure can be parameterized both using global design variables to define the general pattern and local variables to modify the crease shapes, as shown in Figure 5.3d. The global variables are $\boldsymbol{R_i}$, the length of the shortest side of the star; $\boldsymbol{R_e}$, the length of the longest side of the star; and $\boldsymbol{\omega}$, the ratio of thicknesses between the soft hinges and the rigid facets. For the compliant crease geometry, four additional variables are implemented: $\boldsymbol{r}$, the radius of the central hole; $\boldsymbol{\alpha}$, the normalized angle defining the position of the node where the displacement is imposed; $\boldsymbol{h}$, the height of the vertical crease; and $\boldsymbol{l_1}$ and $\boldsymbol{l_2}$, which characterize the width at the tip of the creases of the longest and shortest sides, respectively.

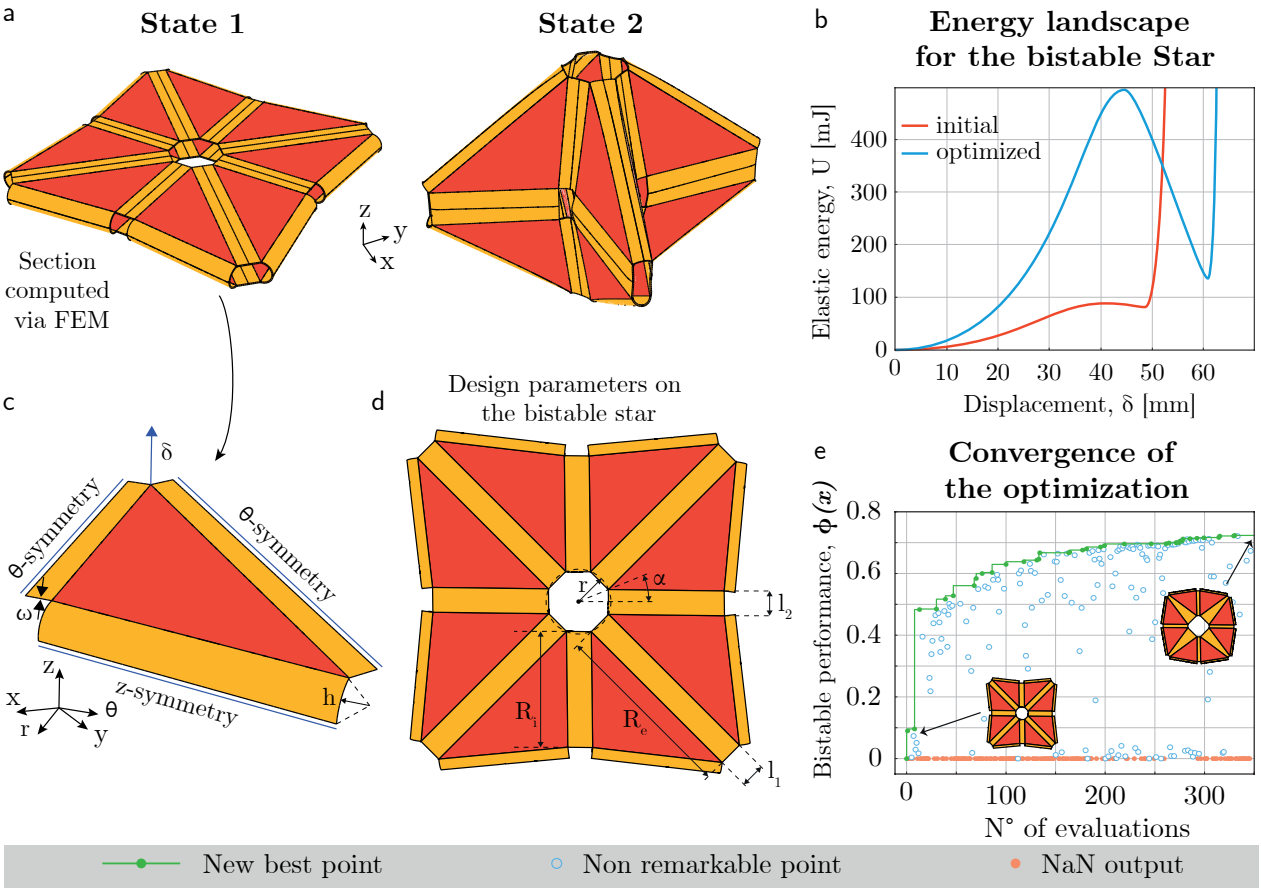

Figure 5.3 **Numerical model of the bistable star origami : a.** Bistable star in both the compact (state 1) and the deployed (state 2) configurations. **b.** An energy-displacement curve exhibiting both the initial and the final shapes of the optimization. **c.** Finite Element model and the associated boundary conditions. **d.** The bistable star parameterized with all the available design variables. **e.** Convergence of the objective function (bistable performance) of the optimization.

An optimization using MADS is conducted with the objective function $\boldsymbol{\phi = f(r, \alpha, l_1, l_2, R_i, R_e)}$. The number of design variables considered in the optimization process can be adapted to the needs of the application for which the bistable star will be used. Optimization is launched from the point $\boldsymbol{x^0 = (13.1, 0.5, 5.0, 5.0, 58.9, 85.9)}$, defining a shape where the width of the creases is uniform across the structure. This initial configuration provides a bistable performance $\boldsymbol{\phi^0 = 9.0\%}$. The lower and upper boundary conditions for the optimization, respectively $\boldsymbol{l_b}$ and $\boldsymbol{u_b}$, are defined by:

— $\boldsymbol{l_b = (5.0, 0.0, 0.0, 0.0, 50.0, 50.0)}$,

— $\boldsymbol{u_b = (35.0, 1.0, 10.0, 10.0, 150.0, 150.0)}$.

After 350 evaluations, the process outputted an improved shape defined by $\boldsymbol{x^* = (26.1, 0.8, 4.3, 3.3, 85.5, 102.2)}$ and an improved bistable performance $\boldsymbol{\phi^* = 72.6\%}$. One can note that none of

the design variables ended up reaching the boundary conditions in the improved configuration. The convergence graph of this optimization is displayed in Figure 5.3e. The plot exhibits a large number of failed evaluations, as is the case for the optimization of the waterbomb. When the optimization is stopped, i.e., after **350** evaluations, the plot exhibits a great increase within the first **50** evaluations and keeps growing until the stopping criterion is reached.

5.3.2 Bistable Kresling Origami Parametrization

Similarly, a numerical model of the Kresling origami pattern is constructed as a blackbox to further test our optimization framework. The model is inspired by a previous project simulating the Kresling pattern [23], but with an improved parametrization that includes design variables controlling the geometry of the compliant hinges.

The Kresling pattern presents two stable states: a deployed one and one compressed along its longitudinal axis (see Figure 5.4a). This associated energy curve displays a relatively shallow energy well. To exhibit bistable behavior, one must keep the polygonal shapes defining the top and bottom geometry unaltered during compression, by clamping the bottom nodes and applying a uniform displacement over the top surface.

While previous work has demonstrated that the Kresling pattern can be parameterized globally by varying the height $\boldsymbol{h}$, the ratio of width between the facets and the hinges $\boldsymbol{\omega}$, the number of sides $\boldsymbol{n}$ for the polygons defining the top and bottom surfaces, and the initial twist $\boldsymbol{\varphi}$ between these same surfaces, crease parameters can be implemented to define the area occupied by the facets on each side of the Kresling. Two variables can be used for each corner of the triangular facets: $\boldsymbol{t_i}$ to control the distance between the corner of the geometry and the corner of the facet, and $\boldsymbol{r_i}$ to control the angle with the $\boldsymbol{xy}$-plane. Each side of the Kresling can be parameterized independently, with additional variables ranging from 2 to $\mathbf{12}.\boldsymbol{n}$.

An optimization is conducted on the Kresling with the general design variable. A total of 250 evaluations and over a week of computation were necessary to go from an initial configuration with a 27% bistable performance to a geometry displaying over 57%. Results could be further improved by implementing the design variable defining compliant creases geometry.

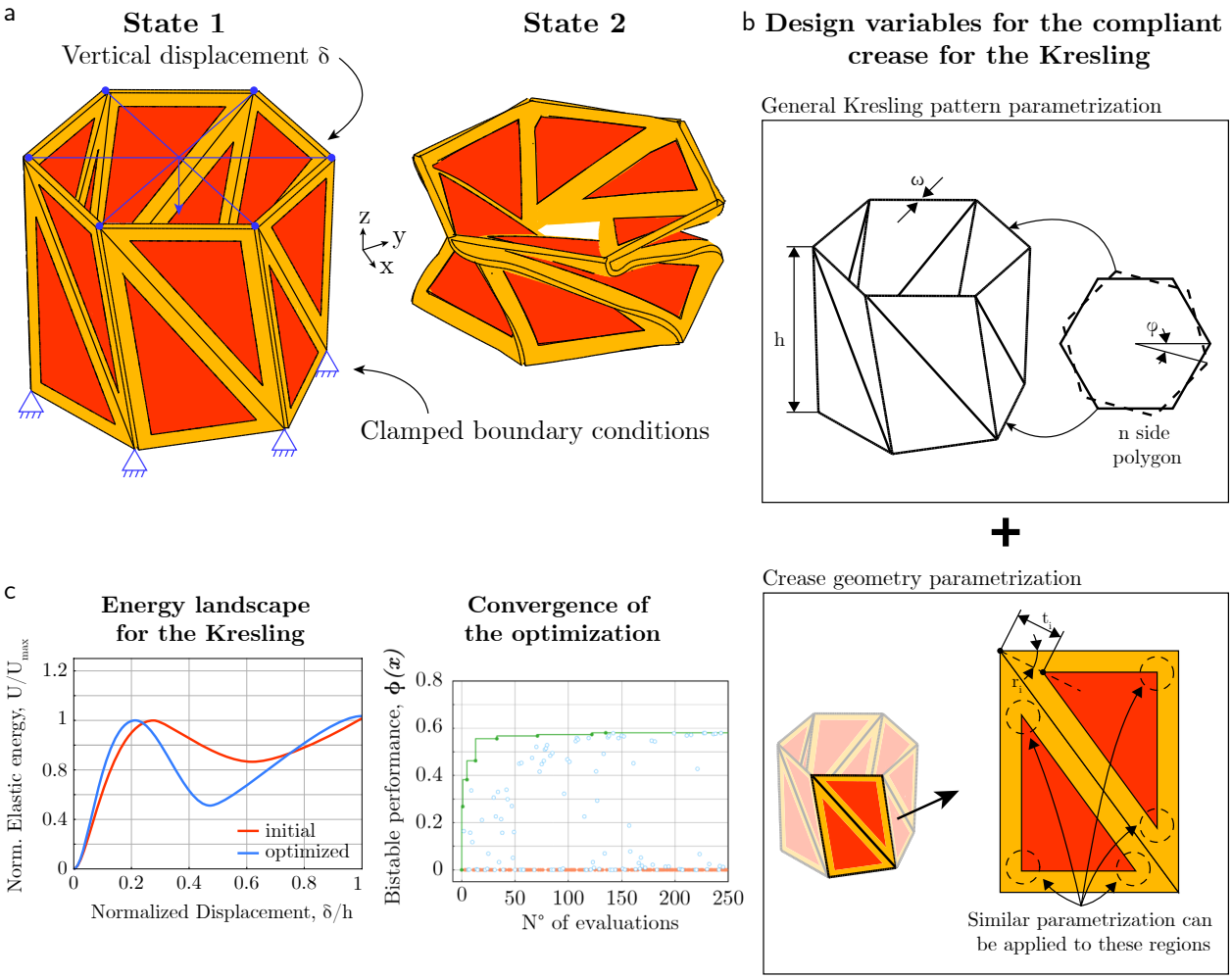

Design variables available : **12.n** variables for the creases and **4** global variables for the pattern

Figure 5.4 **Numerical model of the Kresling origami: a.** Finite Element model of the origami pattern both in the initial deployed state and in the compressed stable configuration. An energy-displacement curve is provided to exhibit the bistable behavior. **b.** A complete parametrization of the structure both in the compliant crease shape and in the general pattern definition. **c.** Convergence and resulting energy curve for an optimization made with the general design variables of the kresling.

CHAPTER 6 CONCLUSION

6.1 Summary of work

In this work, we propose an optimization methodology to improve mechanical performance of multistable origami-inspired structures. The framework relies on coupling a nonlinear finite element blackbox model with the derivative-free optimization algorithm MADS. Our numerical model represents origami structures made of stiff panels connected with softer compliant hinges to allow deformation of the system and is able to output the elastic energy developed during the deployment. A focus was placed on the waterbomb origami pattern as a validation case for our methodology due to its relevance in previous research projects. Using a geometrical parametrization of the folding regions, we were able to modulate the bistable performance, i.e., modify the energy needed to escape certain energy wells of the structures. The results were validated experimentally on 3D-printed, characterized by energy curves results close to those obtained numerically. Implementation of interlacing geometry for 3D printing using TPU and PLA was realized to manufacture test samples.

After optimization, the bistable performance was more than doubled compared to the classical pattern using straight compliant creases. This result was obtained through several optimization cases, both with and without consideration of the limitations arising from the manufacturing method.

We demonstrated that the optimization process can adapt to the needs of the application: the level of energy desired can be implemented as a constraint in the optimization problem. The process is not limited to the waterbomb pattern, and the blackbox model can be substituted for any origami-inspired bistable structure with parameterized geometry.

6.2 Limitations

FEM can accurately simulate the deployment of origami, but fails to converge with geometries developing high levels of energy. The computation fails often happens right before reaching the critical point of instability, $\boldsymbol{U_{max}}$. We need to find a solution to reduce computation failures to close to 0% and return to static nonlinear calculations.

As of now, it seems one cannot reach energetic neutrality in every state. Even with a wider design space, we were not able to surpass $\boldsymbol{\phi = 80\%}$ bistability performance. This limitation may not occur with other origami patterns the residual strain depends on the amplitude of motion of the structure.

Even though experiments validated our numerical results qualitatively, there remains a difference in the measured energy for some of the designs presented. The boundary conditions may vary from the FE model, causing variation when tested experimentally. Experimentation may also be affected

by the rigidity of the link between the samples and the tensile testing machine, as well as by the location where the waterbomb pattern is positioned.

6.3 Future research

The optimization presented in this thesis could be further improved in several aspects. To achieve better results for bistable performance, additional design variables could be implemented, such as the number of cyclic symmetries in the waterbomb origami pattern or the radii of the inner and outer diameters. Categorical variables could also be introduced to control the material of each region independently within the optimization.

To reduce the time taken for optimization, one could include a surrogate model in the optimization process. Surrogate models are functions that provide information similar to that computed by the blackbox function but require less time to compute. This model would be used by the MADS algorithm to give a rough estimate of the blackbox value and guide the process in determining the next evaluation points. The SWOMPS (Sequentially Working Origami Multi-Physics Simulator) [90] package implements the bar and hinge formulation and takes only a few seconds to compute compliant crease origami models. As of now, the model is not fully suitable for our optimization because of a lack of flexibility in the computable designs and a high number of failures when estimating the model. However, the package is regularly updated, and newer versions may provide satisfactory results for a surrogate model.

The process introduced in this thesis is suitable for bistable structures, i.e., systems with only two stable states. One may want to optimize multistable structures with more than two equilibrium states. Three approaches could be tested. First, use a multi-objective optimization, with the objective function being the bistability performance of each state switching. Second, reuse the same optimization framework presented but define a new objective function to capture every energy. This could be defined as the sum of each independent energy barrier, for example. Third, as most multistable origami-inspired structures are designed by assembling bistable building blocks, one could optimize the building blocks and then assemble them into the larger structure.

Finally, the optimization showed that widening the design space helped improve bistability. To enable this, one must improve 3D printing methods to better fabricate the smaller regions of the structure or switch to other manufacturing methods, such as composite laminates.

REFERENCES

[1] Alarie, S., Audet, C., Gheribi, A., Kokkolaras, M., and Le Digabel, S. (2021). Two decades of blackbox optimization applications. EURO Journal on Computational Optimization, 9:100011.

[2] Arnouts, L. I. W., Massart, T. J., De Temmerman, N., and Berke, P. Z. (2019). Computational design of bistable deployable scissor structures: Trends and challenges. Journal of the International Association for Shell and Spatial Structures, 60(1):19–34.

[3] Audet, C., Béchard, V., and Le Digabel, S. (2008). Nonsmooth optimization through Mesh Adaptive Direct Search and Variable Neighborhood Search. Journal of Global Optimization, 41(2):299–318.

[4] Audet, C. and Dennis, Jr., J. (2006). Mesh Adaptive Direct Search Algorithms for Constrained Optimization. SIAM Journal on Optimization, 17(1):188–217.

[5] Audet, C. and Dennis, Jr., J. (2009). A Progressive Barrier for Derivative-Free Nonlinear Programming. SIAM Journal on Optimization, 20(1):445–472.

[6] Audet, C., Hallé-Hannan, E., and Le Digabel, S. (2023). A General Mathematical Framework for Constrained Mixed-variable Blackbox Optimization Problems with Meta and Categorical Variables. Operations Research Forum, 4(12).

[7] Audet, C. and Hare, W. (2017). Derivative-Free and Blackbox Optimization. Springer Series in Operations Research and Financial Engineering. Springer, Cham, Switzerland.

[8] Audet, C., Le Digabel, S., Rochon Montplaisir, V., and Tribes, C. (2022a). Algorithm 1027: NOMAD version 4: Nonlinear optimization with the MADS algorithm. ACM Transactions on Mathematical Software, 48(3):35:1–35:22.

[9] Audet, C., Le Digabel, S., and Saltet, R. (2022b). Quantifying uncertainty with ensembles of surrogates for blackbox optimization. Computational Optimization and Applications, 83:29–66.

[10] Audet, C. and Orban, D. (2006). Finding optimal algorithmic parameters using derivative-free optimization. SIAM Journal on Optimization, 17(3):642–664.

[11] Audet, C., Savard, G., and Zghal, W. (2010). A mesh adaptive direct search algorithm for multiobjective optimization. European Journal of Operational Research, 204(3):545–556.

[12] Bai, Y., Wang, S., Zhou, X., and Beer, M. (2023). Three-dimensional ori-kirigami metamaterials with multistability. Physical Review E, 107(3):035004.

[13] Benouhiba, A., Rougeot, P., Andreff, N., Rabenorosoa, K., and Ouisse, M. (2021). Origami-based auxetic tunable Helmholtz resonator for noise control. Smart Materials and Structures, 30(3):035029.

[14] Booker, A., Dennis, Jr., J., Frank, P., Serafini, D., Torczon, V., and Trosset, M. (1999). A Rigorous Framework for Optimization of Expensive Functions by Surrogates. Structural and Multidisciplinary Optimization, 17(1):1–13.

[15] Boyvat, M., Koh, J.-S., and Wood, R. J. (2017). Addressable wireless actuation for multijoint folding robots and devices. Science Robotics, 2(8).

[16] Brancewicz-Steinmetz, E., Vergara, R., Buzalski, V., and Sawicki, J. (2022). Study of the adhesion between TPU and PLA in multi-material 3D printing. Journal of Achievements in Materials and Manufacturing Engineering, 115(2):49–56.

[17] Brown, N., Varela, K., Ynchausti, C., Howell, L. L., and Magleby, S. P. (2022). Dual-Purpose Lenticular Locking Hinges for Actuation and Stiffening of Deployable Origami Arrays. In Volume 7: 46th Mechanisms and Robotics Conference (MR), International Design Engineering Technical Conferences and Computers and Information in Engineering Conference.

[18] Brunck, V., Lechenault, F., Reid, A., and Adda-Bedia, M. (2016). Elastic theory of origami-based metamaterials. Physical Review E, 93(3):033005.

[19] Chen, T. and Shea, K. (2021). Computational design of multi-stable, reconfigurable surfaces. Materials & Design, 205:109688.

[20] Chen, X. and Kelley, C. (2016). Optimization with hidden constraints and embedded Monte Carlo computations. Optimization and Engineering, 17(1):157–175.

[21] Chung, G., Chae, J., Han, D., Won, S., and Park, Y. (2024). Reprogrammable, recyclable origami robots controlled by magnetic fields. Advanced Intelligent Systems.

[22] Conn, A., Scheinberg, K., and Vicente, L. (2009). Introduction to Derivative-Free Optimization. MOS-SIAM Series on Optimization. SIAM, Philadelphia.

[23] Dalaq, A. S. and Daqaq, M. F. (2022). Experimentally-validated computational modeling and characterization of the quasi-static behavior of functional 3d-printed origami-inspired springs. Materials & Design, 216:110541.

[24] Deleo, A. A., O'Neil, J., Yasuda, H., Salviato, M., and Yang, J. (2020). Origami-based deployable structures made of carbon fiber reinforced polymer composites. Composites Science and Technology, 191:108060.

[25] Dudte, L. H., Choi, G. P. T., and Mahadevan, L. (2021). An additive algorithm for origami design. Proceedings of the National Academy of Sciences, 118(21).

[26] Dudte, L. H., Vouga, E., Tachi, T., and Mahadevan, L. (2016). Programming curvature using origami tessellations. Nature Materials, 15(5):583–588.

[27] Faber, J. A., Arrieta, A. F., and Studart, A. R. (2018). Bioinspired spring origami. Science, 359(6382):1386–1391.

[28] Fang, H., Chang, T.-S., and Wang, K. W. (2019). Magneto-origami structures: engineering multi-stability and dynamics via magnetic-elastic coupling. Smart Materials and Structures, 29(1):015026.

[29] Fang, H., Zhang, Y., and Wang, K. W. (2017). Origami-based earthworm-like locomotion robots. Bioinspiration & Biomimetics, 12(6):065003.

[30] Felton, S. M., Tolley, M. T., Shin, B., Onal, C. D., Demaine, E. D., Rus, D., and Wood, R. J. (2013). Self-folding with shape memory composites. Soft Matter, 9(32):7688–7694.

[31] Feng, F., Dang, X., James, R. D., and Plucinsky, P. (2020). The designs and deformations of rigidly and flat-foldable quadrilateral mesh origami. Journal of the Mechanics and Physics of Solids, 142:104018.

[32] Fermi, E. and Metropolis, N. (1952). Numerical solution of a minimum problem. Los Alamos Unclassified Report LA–1492, Los Alamos National Laboratory, Los Alamos, USA.

[33] Flores, J., Stein-Montalvo, L., and Adriaenssens, S. (2022). Effect of crease curvature on the bistability of the origami waterbomb base. Extreme Mechanics Letters, 57:101909.

[34] Georgakopoulos, S. V., Zekios, C. L., Sattar-Kaddour, A., Hamza, M., Biswas, A., Clark, B., Ynchausti, C., Howell, L. L., Magleby, S. P., and Lang, R. J. (2021). Origami antennas. IEEE Open Journal of Antennas and Propagation, 2:1020–1043.

[35] Gillman, A., Wilson, G., Fuchi, K., Hartl, D., Pankonien, A., and Buskohl, P. (2019). Design of soft origami mechanisms with targeted symmetries. Actuators, 8(1):3.

[36] Gorissen, B., Melancon, D., Vasios, N., Torbati, M., and Bertoldi, K. (2020). Inflatable soft jumper inspired by shell snapping. Science Robotics, 5(42).

[37] Hanna, B. H., Lund, J. M., Lang, R. J., Magleby, S. P., and Howell, L. L. (2014). Waterbomb base: a symmetric single-vertex bistable origami mechanism. Smart Materials and Structures, 23(9):094009.

[38] Hanson, N., Mensah, I. A., Roberts, S. F., Healey, J., Wu, C., and Dorsey, K. L. (2024). Controlling the fold: proprioceptive feedback in a soft origami robot. Frontiers in Robotics and AI, 11.

[39] Holland, A. and Straub, J. (2016). Development of origami-style solar panels for use in support of a mars mission. In Energy Harvesting and Storage: Materials, Devices, and Applications VII, volume 9865, pages 72–77. SPIE.

[40] Imada, R. and Tachi, T. (2022). Geometry and Kinematics of Cylindrical Waterbomb Tessellation. Journal of Mechanisms and Robotics, 14(041009).

[41] Iniguez-Rabago, A. and Overvelde, J. T. B. (2022). From rigid to amorphous folding behavior in origami-inspired metamaterials with bistable hinges. Extreme Mechanics Letters, 56:101881.

[42] Jamalimehr, A., Mirzajanzadeh, M., Akbarzadeh, A., and Pasini, D. (2022). Rigidly flat-foldable class of lockable origami-inspired metamaterials with topological stiff states. Nature Communications, 13(1):1816.

[43] Kim, W., Byun, J., Kim, J.-K., Choi, W.-Y., Jakobsen, K., Jakobsen, J., Lee, D.-Y., and Cho, K.-J. (2019). Bioinspired dual-morphing stretchable origami. Science Robotics, 4(36).

[44] Kuipers, T., Su, R., Wu, J., and Wang, C. C. L. (2022). ITIL: Interlaced topologically interlocking lattice for continuous dual-material extrusion. Additive Manufacturing, 50:102495.

[45] Kuribayashi, K., Tsuchiya, K., You, Z., Tomus, D., Umemoto, M., Ito, T., and Sasaki, M. (2006). Self-deployable *origami* stent grafts as a biomedical application of ni-rich TiNi shape memory alloy foil. Materials Science and Engineering: A, 419(1):131–137.

[46] Lang, R. J., Brown, N., Ignaut, B., Magleby, S., and Howell, L. (2020). Rigidly foldable thick origami using designed-offset linkages. Journal of Mechanisms and Robotics, 12(21106).

[47] Lang, R. J. and Howell, L. (2018). Rigidly foldable quadrilateral meshes from angle arrays. Journal of Mechanisms and Robotics, 10(21004).

[48] Le Digabel, S. and Wild, S. (2024). A taxonomy of constraints in black-box simulation-based optimization. Optimization and Engineering, 25(2):1125–1143.

[49] Lee, M., Miyajima, Y., and Tachi, T. (2023). Designing and analyzing multistable mechanisms using quadrilateral boundary rigid origami. Journal of Mechanisms and Robotics, 16(11008).

[50] Li, S., Stampfli, J. J., Xu, H. J., Malkin, E., Diaz, E. V., Rus, D., and Wood, R. J. (2019). A vacuum-driven origami "magic-ball" soft gripper. In 2019 International Conference on Robotics and Automation (ICRA), pages 7401–7408.

[51] Li, S., Vogt, D. M., Rus, D., and Wood, R. J. (2017). Fluid-driven origami-inspired artificial muscles. Proceedings of the National Academy of Sciences, 114(50):13132–13137.

[52] Liu, C.-X., Wang, X., Liu, W., Yang, Y.-F., Yu, G.-L., and Liu, Z. (2024). A physics-informed neural network for kresling origami structures. International Journal of Mechanical Sciences, 269:109080.

[53] Liu, F., Jiang, X., Wang, X., and Wang, L. (2020). Machine learning-based design and optimization of curved beams for multistable structures and metamaterials. Extreme Mechanics Letters, 41:101002.

[54] Liu, Q., Wang, W., Reynolds, M. F., Cao, M. C., Miskin, M. Z., Arias, T. A., Muller, D. A., McEuen, P. L., and Cohen, I. (2021). Micrometer-sized electrically programmable shape-memory actuators for low-power microrobotics. Science Robotics, 6(52).

[55] Marsden, A., Wang, M., Dennis, Jr., J., and Moin, P. (2007). Trailing-edge noise reduction using derivative-free optimization and large-eddy simulation. Journal of Fluid Mechanics, 572:13–36.

[56] Martinez, R. V., Fish, C. R., Chen, X., and Whitesides, G. M. (2012). Elastomeric Origami: Programmable Paper-Elastomer Composites as Pneumatic Actuators. Advanced Functional Materials, 22(7):1376–1384.

[57] McInerney, J., Paulino, G. H., and Rocklin, D. Z. (2022). Discrete symmetries control geometric mechanics in parallelogram-based origami. Proceedings of the National Academy of Sciences, 119(32).

[58] McKay, M. D., Beckman, R. J., and Conover, W. J. (1979). A comparison of three methods for selecting values of input variables in the analysis of output from a computer code. Technometrics, 21(2):239–245.

[59] McKinnon, K. I. M. (1998). Convergence of the nelder–mead simplex method to a nonstationary point. 9(1):148–158.

[60] Melancon, D., Forte, A. E., Kamp, L. M., Gorissen, B., and Bertoldi, K. (2022). Inflatable Origami: Multimodal Deformation via Multistability. Advanced Functional Materials, 32(35).

[61] Melancon, D., Gorissen, B., García-Mora, C. J., Hoberman, C., and Bertoldi, K. (2021). Multistable inflatable origami structures at the metre scale. Nature, 592(7855):545–550.

[62] Micheletti, A., Giannetti, I., Mattei, G., and Tiero, A. (2022). Kinematic and static design of rigid origami structures: Application to modular yoshimura patterns. Journal of Architectural Engineering, 28(2):04022009.

[63] Misseroni, D., Pratapa, P. P., Liu, K., Kresling, B., Chen, Y., Daraio, C., and Paulino, G. H. (2024). Origami engineering. Nature Reviews Methods Primers, 4(1):1–19.

[64] Murali Babu, S. P., Das, R., Mazzolai, B., and Rafsanjani, A. (2023). Programmable inflatable origami. In 2023 IEEE International Conference on Soft Robotics (RoboSoft), pages 1–6.

[65] Nelder, J. A. and Mead, R. (1965). A simplex method for function minimization. The Computer Journal, 7(4):308–313.

[66] Novelino, L. S., Ze, Q., Wu, S., Paulino, G. H., and Zhao, R. (2020). Untethered control of functional origami microrobots with distributed actuation. Proceedings of the National Academy of Sciences, 117(39):24096–24101.

[67] Overvelde, J. T. B., Weaver, J. C., Hoberman, C., and Bertoldi, K. (2017). Rational design of reconfigurable prismatic architected materials. Nature, 541(7637):347–352.

[68] Peng, Y., Niloy, I., Kam, M., Celli, P., and Plucinsky, P. (2024). Programming bistability in geometrically perturbed mechanical metamaterials. Physical Review Applied, 22(1):014073.

[69] Peraza Hernandez, E. A., Hartl, D. J., and Lagoudas, D. C. (2016). Kinematics of origami structures with smooth folds. Journal of Mechanisms and Robotics, 8(6).

[70] Rus, D. and Tolley, M. T. (2018). Design, fabrication and control of origami robots. Nature Reviews Materials, 3(6):101–112.

[71] Schenk, M. and Guest, S. D. (2013). Geometry of miura-folded metamaterials. Proceedings of the National Academy of Sciences, 110(9):3276–3281.

[72] Shan, S., Kang, S. H., Raney, J. R., Wang, P., Fang, L., Candido, F., Lewis, J. A., and Bertoldi, K. (2015). Multistable architected materials for trapping elastic strain energy. Advanced Materials, 27(29):4296–4301.

[73] Silverberg, J. L., Evans, A. A., McLeod, L., Hayward, R. C., Hull, T., Santangelo, C. D., and Cohen, I. (2014). Using origami design principles to fold reprogrammable mechanical metamaterials. Science, 345(6197):647–650.

[74] Silverberg, J. L., Na, J.-H., Evans, A. A., Liu, B., Hull, T. C., Santangelo, C. D., Lang, R. J., Hayward, R. C., and Cohen, I. (2015). Origami structures with a critical transition to bistability arising from hidden degrees of freedom. Nature Materials, 14(4):389–393.

[75] Suzuki, H. and Wood, R. J. (2020). Origami-inspired miniature manipulator for teleoperated microsurgery. Nature Machine Intelligence, 2(8):437–446.

[76] Tachi, T. (2009). Simulation of rigid origami. In Origami 4: Fourth International Meeting of Origami Science, Mathematics, and Education.

[77] Tachi, T. (2011). Rigid-foldable thick origami. In Origami 5 : Fifth International Meeting of Origami Science, Mathematics, and Education.

[78] Torczon, V. (1997). On the convergence of pattern search algorithms. SIAM Journal on Optimization, 7(1):1–25.

[79] Treml, B., Gillman, A., Buskohl, P., and Vaia, R. (2018). Origami mechanologic. Proceedings of the National Academy of Sciences, 115(27):6916–6921.

[80] Wang, C., Zhang, D., Li, J., Li, Y., and Zhang, X. (2024). Deployment dynamics of thick panel miura-origami. Aerospace Science and Technology, 144.

[81] Wang, X., Qu, H., Li, X., Kuang, Y., Wang, H., and Guo, S. (2023). Multi-triangles cylindrical origami and inspired metamaterials with tunable stiffness and stretchable robotic arm. PNAS Nexus, 2(4).

[82] Wu, S., Ze, Q., Dai, J., Udipi, N., Paulino, G. H., and Zhao, R. (2021). Stretchable origami robotic arm with omnidirectional bending and twisting. Proceedings of the National Academy of Sciences, 118(36):e2110023118.

[83] Wu, W. and You, Z. (2011). A solution for folding rigid tall shopping bags. Proceedings of the Royal Society A: Mathematical, Physical and Engineering Sciences.

[84] Yang, M., Grey, S. W., Scarpa, F., and Schenk, M. (2023). Large impact of small vertex cuts on the mechanics of origami bellows. Extreme Mechanics Letters, 60:101950.

[85] Ye, H., Liu, Q., Cheng, J., Li, H., Jian, B., Wang, R., Sun, Z., Lu, Y., and Ge, Q. (2023). Multimaterial 3d printed self-locking thick-panel origami metamaterials. Nature Communications, 14(1):1607.

[86] Ze, Q., Wu, S., Dai, J., Leanza, S., Ikeda, G., Yang, P. C., Iaccarino, G., and Zhao, R. R. (2022). Spinning-enabled wireless amphibious origami millirobot. Nature Communications, 13(1):3118.

[87] Zhang, H., Zhu, B., and Zhang, X. (2018). Origami kaleidocycle-inspired symmetric multistable compliant mechanisms. Journal of Mechanisms and Robotics, 11(11009).

[88] Zhang, Q., Fang, H., and Xu, J. (2023). Tunable dynamics in yoshimura origami by harnessing pneumatic pressure. Journal of Sound and Vibration, 544:117407.

[89] Zhou, H., Fang, H., Liu, Z., and Xu, J. (2024). SMA-origami coupling: online configuration switches and stability property modulation. International Journal of Smart and Nano Materials, 15(1):21–41.

[90] Zhu, Y. and Filipov, E. T. (2020). A bar and hinge model for simulating bistability in origami structures with compliant creases. Journal of Mechanisms and Robotics, 12(21110).

[91] Zhu, Y. and Filipov, E. T. (2021). Sequentially Working Origami Multi-Physics Simulator (SWOMPS): A Versatile Implementation. In Volume 8B: 45th Mechanisms and Robotics Conference (MR), International Design Engineering Technical Conferences and Computers and Information in Engineering Conference.

[92] Zhu, Y. and Filipov, E. T. (2024). Large-scale modular and uniformly thick origami-inspired adaptable and load-carrying structures. Nature Communications, 15(1):2353.

[93] Zhu, Y., Schenk, M., and Filipov, E. T. (2022). A review on origami simulations: From kinematics, to mechanics, toward multiphysics. Applied Mechanics Reviews, 74(3):030801.

[94] Zirbel, S. A., Lang, R. J., Thomson, M. W., Sigel, D. A., Walkemeyer, P. E., Trease, B. P., Magleby, S. P., and Howell, L. L. (2013). Accommodating thickness in origami-based deployable arrays1. Journal of Mechanical Design, 135(111005).

[95] Zirbel, S. A., Trease, B. P., Thomson, M. W., Lang, R. J., Magleby, S. P., and Howell, L. H. (2015). HanaFlex: a large solar array for space applications. In Micro- and Nanotechnology Sensors, Systems, and Applications VII, volume 9467, pages 179–187. SPIE.